International Communications in Heat and Mass Transfer 179 (2026) 112221

Contents lists available at ScienceDirect

International Communications in Heat and Mass Transfer

journal homepage: www.elsevier.com/locate/ichmt

Evaluation of new cascade sustainable multioutput energy system for hydrogen/fresh water/power production from industrial waste: Impact of working fluid and heat source conditions

Mohamed Ashraf [a,b], Sameh Nada [a,b], Hamdy Hassan [a,c,*]

[a] Department of Energy Resources Engineering, Egypt-Japan University of Science and Technology, Alexandria 21934, Egypt
[b] Department of Mechanical Engineering, Benha Faculty of Engineering, Benha University, Benha, Egypt
[c] Mechanical Power Engineering Department, Faculty of Engineering, Assiut University, Assiut 71516, Egypt

ARTICLE INFO

Keywords:
Waste steam
Hydrogen production
Heat recovery
Poly-generation system
PEM electrolysis
HDH desalination

ABSTRACT

This study assesses a poly-generation system, driven by low-grade industrial waste steam, that is electrically and hydraulically self-sufficient — its hydrogen electrolyzer draws power and feedwater entirely from upstream subsystems within the cascade rather than from grid electricity or external freshwater supply — while depending on a continuous waste-steam stream, seawater feed, and auxiliary cooling infrastructure as its external thermal and material boundary conditions. The system features a four-stage thermodynamic cascade comprising an Organic Rankine Cycle (ORC), a Thermoelectric Generator (TEG), a Humidification-Dehumidification (HDH) desalination unit, and a Proton Exchange Membrane (PEM) electrolyzer. The study was carried out for the ORC working fluids R245fa, Cyclopentane, and n-Pentane, at different waste steam temperatures and qualities. A rigorous mathematical model was developed in MATLAB, with each subsystem independently validated against dedicated experimental datasets; full four-stage cascade validation was not attempted because no equivalent integrated experimental system exists in the literature. The results show that using R245fa resulted in significant operational instability, with a 16% power drop. Cyclopentane eliminates the transition penalty and ensures a smooth, monotonic rise in power across the full temperature range. Under the highest steam operating conditions (200 °C, saturated vapor), the system utilizing Cyclopentane delivers a maximum net power of 998.48 kW, a peak hydrogen production rate of 22.12 kg/h, and an overall system efficiency of 12.82%, representing a 25% improvement over the R245fa baseline. A complementary exergy analysis reveals that Cyclopentane also achieves the highest overall second-law efficiency (18.20%). Furthermore, component-level assessments identify the HDH unit as the primary thermodynamic bottleneck with the lowest exergetic efficiency (0.19%). In contrast, the PEM electrolyzer achieves the highest (>73%), confirming the rational allocation of high-quality electrical exergy toward hydrogen production. Simultaneously, the HDH unit secures a substantial freshwater surplus of 1948 L/h beyond the electrolyzer's consumption. The study highlights a strategic trade-off: while saturated steam maximizes electrical output, lower steam quality (0.8) maximizes the Energy Utilization Factor of a peak of 39.23%. Techno-economic and environmental assessments confirm the system's viability; utilizing Cyclopentane at 200 °C minimizes the Levelized Cost of Hydrogen (LCOH) to an optimal 1.783 USD/kg, yielding a 20-year Net Present Value (NPV) of 4967.5 kUSD with a rapid payback period (PBP) of 2.49 yr, while mitigating 3775.8 tons of CO2 annually.

1. Introduction

As the world faces the serious impacts of fossil fuel depletion, climate change, and increased CO_2 emissions, shifting to sustainable energy sources has become essential. Hydrogen fuel is gaining recognition as a viable and sustainable energy carrier. Its high energy content, versatile storage capabilities, and carbon-neutral burning make hydrogen a promising option for reducing carbon emissions across multiple sectors [1]. However, the production of green hydrogen via water electrolysis faces two major obstacles. The first is the substantial energy intensity required to split water [2]. PEM electrolysis is a widely used low-

* Corresponding author at: Department of Energy Resources Engineering, Egypt-Japan University of Science and Technology, Alexandria 21934, Egypt.
E-mail address: hamdy.aboali@ejust.edu.eg (H. Hassan).

https://doi.org/10.1016/j.icheatmasstransfer.2026.112221

Available online 3 August 2026

Nomenclature

A	Area, m^2
CCG	Carbon Credit Gain, USD/yr
d	Fin spacing, mm
D_h	Hydraulic Diameter, mm
E_{act}	Activation energy, kJ/mol
ex	Specific exergy, J/kg
$\dot{E}x_{dest}$	The exergy destruction rates, kW
EF_{grid}	grid emission factor, $kgCO_2/kWh$
F	Faraday's constant, C/mol
f_{misc}	miscellaneous factor, %
G_m	Mass velocity, $kg/m^2 \bullet s$
ΔG	Gibbs Free Energy, $kJ/kmol$
H	Height, mm
ΔH	Enthalpy change, $kJ/kmol$
h	Specific enthalpy, kJ/kg
h_{conv}	Convective heat transfer coefficient, $W/m^2 \bullet K$
I	Electrical Current, A
J	Current Density, A/m^2
J_0	Exchange current density, A/m^2
J^{ref}	Pre-exponential factor, A/m^2
K	Thermal conductance, W/K
k	Thermal conductivity, $W/m \bullet K$
L	Length, mm
M_{H2}	annual hydrogen production, kg
$\dot{m}$	Mass flow rate, kg/s
M_{CO2}^{mit}	annual mitigated carbon mass, kg/yr
n	Year index/ Number of fins, –
N	TEG modules number, –
n_{pn}	Thermocouple number, –
$\dot{N}$	Molar flow rate, mol/s
N_{cells}	Number of electrolysis cells, –
Nu	Nusselt Number, –
P	Pressure, kPa
Pr	Prandtl number, –
P_r	Reduced pressure, –
$\dot{Q}$	Heat Transfer Rate, kW
r	Discount rate, %
R	Thermal Resistance, K/W
R_{load}	Electrical Load Resistance, Ω
R_{pn}	TEG Internal Resistance, Ω
$R''_{t,c}$	specific contact resistance, $m^2 \bullet K/W$
Re	Reynolds Number, –
R	Universal gas constant, $J/mol.K$
R_{PEM}	total membrane resistance, $\Omega.m^2$
r	Discount rate, %
ΔS	Entropy change, $J/mol.K$
T	Temperature, $^\circ C$ or K
t	thickness, mm
V	Voltage, V
V_0	Reversible potential, V
V_{act}	Irreversible overpotential, V
V_{ohm}	Ohmic loss, V
W	Specific work, kJ/kg
$\dot{W}$	Electrical Power, kW
x	Steam quality, –
Z	Correction Factor, –
Z_k	equipment costs, USD

Greek symbol

α	Seebeck coefficient, V/K
δ	thickness, m
ε	Heat exchanger effectiveness, %
η	efficiency, %
λ	Membrane water content, –
μ	Dynamic viscosity, Pa.s
ρ	Electrical resistivity, $\Omega.m$
σ	Ionic conductivity, S/m
ω	Specific humidity, kg_v/kg_{da}
ϕ	Relative humidity, %
ψ	The exergetic efficiency, %

Subscripts

APTD	Approach Point Temperature
act	Activation
b	Base
c	Cold
CF	Coolant fluid
cons	Consumption
cond	Condenser
conv	Convection
D	Dehumidifier
DSH	Degree of Superheat
eff	effective
evap	Evaporation
ex.steam	Exhausted steam
f	Fin
fresh	Freshwater
g	Gas
gen	generator
h	Hot
H	Humidifier
i	Anode/ cathode
in	Inlet
l	liquid
n	n-type semiconductor
net	Net value
ohm	ohmic
p	Pump/p-type semiconductor
PPTD	Pinch Point Temperature
pn	Pn couple
req	Required
s	Isentropic
sat	Saturation
sw	Seawater
t	Turbine
th	Thermal

Abbreviations

CAOW	Closed-Air-Open-Water
CF	Coolant Fluid
CNS	Central Nervous System
COG	Coke Oven Gas
CRF	Capital Recovery Factor
CO_2	Carbon Dioxide Gas
CWOA	Closed-Water-Open-Air
CAPEX	Capital expenditures
EUF	Energy Utilization Factor
GOR	Gain Output Ratio
GWP	Global Warming Potential
H_2	Hydrogen Gas
HDH	Humidification Dehumidification
HHV	Higher Heating Value
HX	Heat Exchanger
LCOH	Levelized Cost of Hydrogen
LHV	Lower Heating Value
MD	Membrane Distillation

MED	Multi-Effect Distillation	PBP	Payback Period
MSF	Multi-Stage Flash Distillation	*RO*	Reverse Osmosis
MR	Mass Flow Rate Ratio	*RR*	Recovery Ratio
NGL	Natural Gas Liquids	*SOEC*	Solid Oxide Electrolysis Cells
NPV	Net Present Value	SWOG	steelwork off-gas
ORC	Organic Rankine Cycle	*TEG*	Thermoelectric Generator
ODP	Ozone depletion potential	TBT	Top Brine Temperature
OPEX	Operational expenditures	*TRN*	Thermal Resistance Network
PEM	Proton Exchange Membrane	VFD	Variable Frequency Drive
PID	Proportional-Integral-Derivative	*WHR*	Waste Heat Recovery

temperature method (50–80 °C), which offers operational flexibility but incurs high operational costs due to an energy consumption rate of approximately 4.8 kWh/m3 [3,4]. Alternatively, Solid Oxide Electrolysis Cells (SOEC), which utilize high-temperature steam (600–1000 °C) to reduce electrical demand to under 3kWh/m3 [5–7]. Both technologies rely heavily on sustainable power inputs to remain economically and environmentally viable [6–8]. Recent advancements in hybrid polygeneration systems have further underscored the importance of integrating renewable energy with green hydrogen production to enhance system sustainability and resilience [9,10].

The second, often overlooked barrier is the requirement for a stable supply of high-purity water resources under immense global stress. Water scarcity is a critical challenge of the 21st century [11,12]. Simultaneously, the industrial sector dissipates a vast amount of energy as waste heat [13,14]. This WHR resource offers distinct advantages over intermittent renewables like solar or wind, providing a consistent baseload energy supply without extensive land requirements [15,16].

Research into WHR has traditionally followed distinct paths. The first focuses on converting thermal energy into electricity. TEGs are solid-state devices that convert temperature gradients directly into electricity through the Seebeck effect [17]. They are favored for their compactness, reliability, and lack of moving parts [18–20]. However, widespread adoption is hindered by challenges in maintaining temperature gradients [21–23] and low thermal efficiencies (4–7%) [24,25]. Recent optimizations include metastructure heat sinks [26] and large-scale modular arrays [27,28]. For large-scale applications, thermodynamic cycles such as ORCs are preferred. By utilizing organic fluids with low boiling points, ORCs efficiently recover low-to-medium grade heat [29–31], achieving efficiencies of 2–19% [32–34].

A second research stream uses low-grade heat to address water scarcity through thermal desalination. Technologies such as HDH [35–37], Membrane Distillation (MD) [38], Multi-Effect Distillation (MED) [39] effectively utilize recovered heat without additional fuel consumption. The HDH process is particularly well-suited for low-grade waste heat, as it mimics the natural hydrological cycle [35]. The selection of the HDH process for such systems is increasingly supported by its high adaptability for lightweight and off-grid applications, where parametric optimization can significantly boost freshwater productivity [40].

A third, more advanced research stream has focused on directly integrating waste-heat power generation with hydrogen electrolysis. Lümmen et al. [41] studied the integration of an ORC to power a PEM. Similarly, Parham et al. [42] analyzed a multi-generation system using an ORC and an absorption heat transformer to produce power for a PEM, demonstrating that H2 production rates increased with the waste heat temperature. Other studies focused on SOEC, which can utilize waste heat for both power and steam generation [43,44]. Significantly, a few studies have proposed complex multi-generation systems—for example, Ishaq et al. [45] studied a system that used a steam RC, ORC, and a MED system to produce electricity, freshwater, and hydrogen, but relied on a complex thermochemical Cu—Cl cycle. Even more complex integrations have been recently investigated. Shaofu et al. [46] studied a multi-generation system recovering industrial flue gas to produce H_2, CO2, power (via Steam Rankine Cycle, ORC, and TEG), freshwater (via Multi-Stage Flash Distillation (MSF)), and cooling. Similarly, Noorbakhsh et al. [47] analyzed a system primarily powered by a diesel engine, which integrated a PEM with Reverse Osmosis (RO) and MSF desalination units. Furthermore, harnessing waste heat from industrial or marine sources to drive secondary power cycles is a proven strategy for improving thermodynamic efficiency [9].

More recently, several advanced polygeneration studies have further extended the complexity and scope of multi-generation systems. Lin et al. [48] proposed a natural gas-based polygeneration system integrating cryogenic NGL recovery, air turbines, ORC, and a PEM electrolyzer for simultaneous production of NGLs, electricity, hydrogen, and thermal outputs. Multi-objective optimization using XGBoost machine learning yielded energy and exergy efficiencies of 74.41% and 65.26%, respectively, demonstrating the potential of data-driven approaches for high-grade energy system design.

Shaersaikai et al. [49] presented a geothermal-LNG cascaded polygeneration system for power, hydrogen, and freshwater production, employing Grey Wolf Optimization and Random Forest machine learning to achieve a unit specific product cost of 5.37 USD/GJ and a NPV of 15.48 MUSD.

Alamri et al. [50] proposed a machine-learning-optimized multi-generation system driven by recovered Coke Oven Gas (COG), integrating ORC, Kalina cycle, MED desalination, and LNG vaporization to simultaneously produce electricity, heating, cooling, and freshwater, achieving an exergy efficiency of 40.30% through Ant Lion Optimizer-based optimization. In a complementary effort, Alamri et al. [51] introduced a steelwork off-gas (SWOG)-fueled polygeneration system coupling a CO_2 transcritical cycle, ORC, ammonia Rankine cycle, MED desalination, and PEM electrolyzer, attaining overall energy and exergy efficiencies of 73.04% and 31.18%, respectively, with a short payback period of 2.6 years.

More recently, Ben Hamida et al. [52] proposed a solar-driven polygeneration system integrating a supercritical CO_2 cycle, compressed air energy storage (CAES), and a PEM electrolyzer for green hydrogen production. Through the combined application of Grey Wolf Optimization and artificial neural networks, the system achieved an exergy efficiency of 47.9% and a net power output of 76.3 MW. Their study further highlights the growing interest in integrating hydrogen production with advanced multi-generation architectures and intelligent energy management strategies.

While these studies represent significant advances in waste-gas-driven polygeneration — particularly the inclusion of advanced optimization algorithms and comprehensive exergy-economic analysis — they rely on combustible industrial off-gases as primary energy sources and employ complex multi-cycle architectures that may not be applicable to facilities with only low-grade saturated steam availability. Furthermore, neither study addresses the thermodynamic instability arising from subcritical-to-transcritical regime crossings in the ORC working fluid — a critical design challenge for variable-temperature waste heat recovery systems.

A comprehensive review of the literature reveals that while “Waste Heat to Power” (via ORC or TEG), “Waste Heat to Water” (via HDH, MD,

MED, or MSF), and "Waste Heat to Hydrogen" (via PEM or SOEC) have been widely explored as isolated or partially integrated concepts, a critical and practical research gap persists. Many existing multi-generation systems are either (a) reliant on high-grade heat sources [43], (b) exceptionally complex [45], or (c) lack a self-sufficient, cascaded feedstock loop (power and water) specifically designed for a PEM electrolyzer. Consequently, they often rely on non-electrolytic methods [45] or complex desalination technologies like MSF and RO [46,47] rather than a synergistically integrated (HDH) unit.

To the best of the authors' knowledge, no prior study has proposed or analyzed a fully integrated poly-generation system in which a single low-grade industrial waste steam stream is thermodynamically cascaded through four sequential stages — ORC, TEG, HDH, and PEM — such that each stage extracts only the energy appropriate to its thermodynamic quality. To explicitly position this contribution against the existing literature [48–51], the novelty of the present work is established across three distinct and interconnected dimensions:

First, a thermodynamically exhaustive 4-stage single-stream cascade architecture featuring TEG integration. While recent sophisticated studies rely on high-grade combustible fuels such as natural gas [48] or industrial off-gases [50,51], the proposed architecture is specifically designed to valorize low-grade saturated steam with no supplementary heat input. The steam first delivers its highest-grade latent heat to the ORC evaporator. The partially condensed steam then flows across the TEG array, where the Seebeck effect harvests the residual temperature gradient. The further-degraded wet steam enters the HDH unit, driving seawater evaporation to the optimal Top Brine Temperature (TBT) that maximizes the Gain Output Ratio (GOR). Finally, the exhaust stream preheats the HDH-produced distillate to the PEM electrolyzer's optimal 80 °C. Crucially, the inclusion of the TEG acts as a direct thermal bridge that captures intermediate thermal gradients fundamentally discarded in recent ORC-desalination or ORC-PEM configurations [48–51], maximizing exergy recovery from a single low-grade source.

Second, a 100% closed loop and self-sufficient feedstock system for green hydrogen production. Although recent polygeneration frameworks successfully co-produce freshwater and hydrogen [49–51], they typically treat these as parallel outputs or require complex geographical constraints (e.g., simultaneous geothermal and LNG availability [49]), often relying on external water infrastructure. In contrast, the electrical output of the ORC and TEG subsystems serves as the sole power source for the PEM electrolyzer, while the freshwater produced by the HDH unit serves as its sole water feedstock. This internal closure ensures the system perfectly matches the strict ultra-pure water demands of the PEM, eliminating any dependence on external freshwater supply or grid electricity.

Third, a physics-driven characterization of fluid criticality instability. The most recent advanced multi-generation frameworks [48–51] rely exclusively on steady-state, black-box machine learning algorithms (e.g., XGBoost, Random Forest) for system optimization. While mathematically robust, these approaches inherently overlook physical transient behaviors. The present work addresses this critical gap by explicitly characterizing the hidden thermodynamic instability that occurs when the heat source temperature crosses the working fluid's critical temperature, resulting in a sharp, non-monotonic drop in net power output. By systematically evaluating three working fluids (R245fa, n-Pentane, and Cyclopentane) across a 90–200 °C range and inlet steam qualities of 0.8 and 1.0, this analysis demonstrates that fluid selection is not merely a performance parameter but a system stability criterion, ensuring actual operational reliability under fluctuating industrial thermal loads—a factor entirely missed by standard data-driven optimizations.

Collectively, these contributions advance the state-of-the-art by addressing critical gaps in recent multigeneration studies. While existing literature predominantly treats ORC, TEG, and desalination as separate or binary subsystems, this proposed four-stage cascade architecture creates a synergistic link; the TEG unit successfully captures the residual thermal gradient—which is traditionally dissipated in standard cycles—converting it into supplementary direct-current power while strategically pre-conditioning the thermal fluid to match the strict downstream demands of the HDH and PEM units. Ultimately, this framework provides a precise blueprint for converting an environmental liability (waste steam) into a reliable, operationally self-sufficient matrix of electricity, freshwater, and green hydrogen.

Unlike references [48–51], which optimize ORC/Kalina/CO_2-cycle polygeneration architectures using black-box machine-learning algorithms without addressing subcritical–transcritical fluid instability or a fully closed PEM feedstock loop, the present study is, to the authors' knowledge, the first to combine all three elements — TEG-augmented cascading, closed-loop feedstock self-sufficiency, and physics-based fluid-stability characterization — within a single low-grade waste-steam framework.

2. Physical model description

This study proposes a self-sufficient poly-generation system for clean hydrogen production from a single low-grade industrial exhaust steam source (90–200 °C). The system requires no external electricity or freshwater supply once operating; the waste steam, seawater feed, and auxiliary cooling-water circuit constitute its necessary external boundary conditions rather than internally generated resources.

2.1. System cascade and coupling logic

The system operates as a four-stage thermodynamic cascade. In this configuration, the exhaust steam progressively surrenders its thermal energy, with each stage's outlet condition defining the next stage's inlet boundary (Fig. 1).

Stage 1: the exhaust steam (State 5, $x_5 = 0.8$–1) delivers its highest-grade latent heat to the ORC evaporator for primary electricity generation. The outlet steam quality is actively controlled to $x_6 = 0.5$, providing a fixed thermal boundary condition for all downstream stages, regardless of upstream temperature. The fixed outlet steam quality $x_6 = 0.5$ is maintained through a dedicated closed-loop control architecture. Temperature and pressure transducers installed at the evaporator's steam exhaust provide real-time feedback to a Proportional-Integral-Derivative (PID) controller. This controller directly regulates a Variable Frequency Drive (VFD) attached to the ORC working fluid pump, which serves as the primary actuator. By dynamically modulating the organic fluid mass flow rate ($\dot{m}_{ORC}$), the control loop ensures that the exact amount of thermal energy is extracted to partially condense the steam to the target quality. Furthermore, this control mechanism is thermodynamically feasible across the entire evaluated temperature spectrum (90–200 °C). Although the steam's latent heat of vaporization decreases as the source temperature rises, the active modulation of $\dot{m}_{ORC}$ continuously matches the changing thermal load. This guarantees that the required heat transfer is consistently met without causing full condensation, thereby securing stable inlet conditions for the downstream TEG array.

Stage 2: the wet steam at $x_6 = 0.5$ flows across the TEG array, where the residual temperature gradient drives secondary electricity generation via the Seebeck effect. The steam exits at a quality of x_7, which varies with source temperature. In stage 3,the partially condensed steam (State 7) enters the seawater heat exchanger (HX-1), where its residual latent heat heats the seawater feed to the TBT— the thermodynamically optimal condition for maximum GOR. Finally, in Stage 4, the exhaust stream (State 8) passes through a terminal heat exchanger (HX-2), recovering residual thermal energy to preheat the HDH-produced distillate to the PEM optimal operating temperature (80 °C) without external heating. The combined DC power from the ORC and TEG then drives the PEM electrolyzer. Table 1 summarizes the coupling variables and inter-stage boundary conditions.

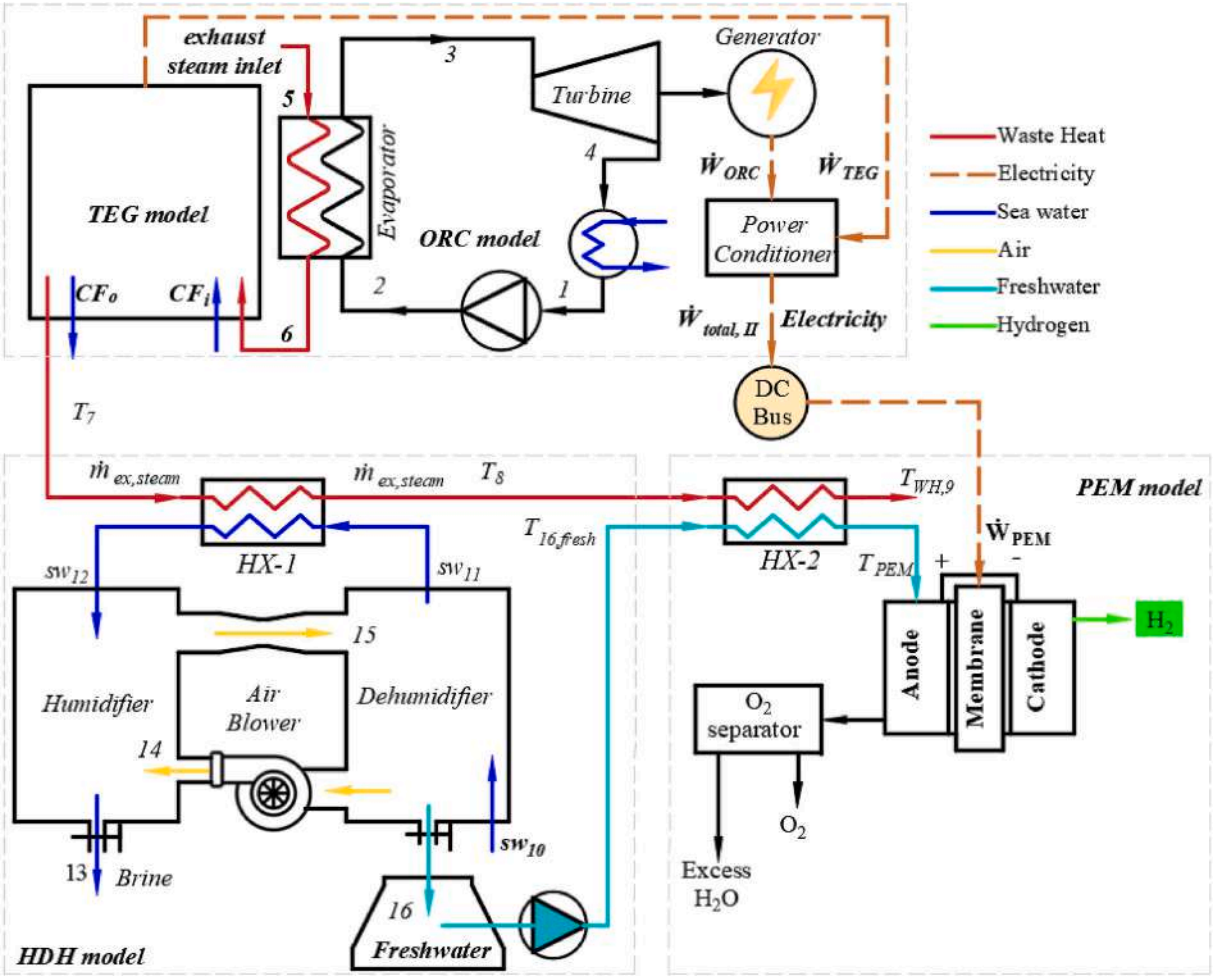

Fig. 1. Schematic diagram of the proposed integrated poly-generation system.

Table 1
Cascade coupling variables and inter-stage boundary conditions.

Stage	Subsystem	Key Input	(Output)	Energy Role
1	ORC	Steam: T_5=90–200 °C x_5=0.8, 1	x_6= 0.5 (controlled)	Primary power generation
2	TEG	Steam: x_6=0.5	x_7(temperature-dependent)	Secondary power generation
3	HDH	x_7, Seawater 25 °C	x_8	Freshwater production
4	PEM	x_8, Distillate	x_9 + H_2 output	H_2 production + preheating

Table 2
Comparative properties of the selected ORC working fluids [53].

Property	R245fa	n-Pentane	Cyclopentane
Critical Temperature (°C)	154.01	196.55	238.57
Critical Pressure (bar)	36.51	33.70	45.15
Normal Boiling Point (°C)	15.14	36.06	49.25
GWP (100-yr)	1030	~5	~5
ODP	0	0	0
ASHRAE Safety Group	B1	A3	A3
Fluid Type	Dry	Dry	Dry
Regulatory Status	F-Gas Phase-down	Permitted	Permitted

2.2. Waste heat recovery system

2.2.1. ORC subsystem

The ORC unit constitutes the first energy recovery stage. The exhaust steam (State 5) enters the evaporator and transfers thermal energy to a closed-loop organic working fluid, which expands through a turbine to drive the generator. Dry organic fluids are exclusively selected to eliminate the risk of liquid droplet formation and associated turbine erosion. Three candidates are evaluated against a multi-criteria framework (Table 2). R245fa (Baseline) widely referenced in literature, but subject to regulatory phase-down due to its high GWP (1030). n-Pentane & Cyclopentane natural hydrocarbons with near-zero GWP (~5), offering a sustainable alternative. The critical thermodynamic differentiator is the critical temperature. As the heat source spans 90–200 °C, R245fa and n-Pentane undergo a subcritical-to-transcritical transition across this range, whereas Cyclopentane ($T_{critical}$ = 238.57 °C) remains entirely within the subcritical regime, ensuring greater operational stability. Cyclopentane's sub-atmospheric condenser pressure necessitates hermetically sealed turbomachinery, vacuum-grade shaft seals, and continuous non-condensable gas removal to mitigate explosion risk from air in-leakage (ASHRAE A3 classification) [53]. Furthermore, while cyclopentane is not highly toxic, acute exposure to vapor concentrations exceeding 2000 ppm can induce Central Nervous System (CNS) depression. Therefore, industrial deployment mandates continuous ambient gas monitoring, ATEX-rated explosion-proof environments, and forced ventilation systems to mitigate both flammability and inhalation risks.

2.2.2. TEG subsystem

The TEG subsystem constitutes the second recovery stage, receiving wet steam ($x_6 = 0.5$) from the ORC evaporator outlet. An optimized 12 × 833 module arrangement — selected from a systematic comparison of four configurations (100 × 100, 50 × 200, 25 × 400, and 12 × 833) with an identical total of 10,000 modules — was chosen because it yielded the highest electrical power output and overall system efficiency while maintaining a practical duct geometry and maximizing latent heat extraction. The higher module count per duct (833) maximizes steam residence time for effective condensation, while the 12 parallel ducts ensure uniform steam distribution [33,34].

The 10,000 commercial SP1848–27145 TEG modules [54] are distributed in a serpentine (zigzag) arrangement across the 12 ducts (Fig. 2a), dimensioned to match the heat transfer area required by the 5 kg/s steam flow rate. A Thermal Resistance Network (TRN) resolves the local thermal path into steam-side convection, heat sink [55], contact interface, and internal module resistances (Fig. 2b).

The cold-side coolant circuit uses a closed-loop intermediate freshwater system (treated water) to prevent corrosive degradation of the aluminum heat sinks that would result from direct seawater cooling. To continuously reject the absorbed thermal energy and maintain a stable cold-junction temperature, this closed-loop freshwater is pumped through an auxiliary industrial cooling tower. This ultimate heat rejection mechanism operates independently of the main thermodynamic cascade, thus preserving the defined boundary conditions. The steam releases its second portion of latent heat through this stage, exiting at quality x_7 to the HDH unit.

The proposed 10,000-module array represents a substantial scale-up from an individually validated commercial module to a full industrial installation, and three practical integration considerations beyond the

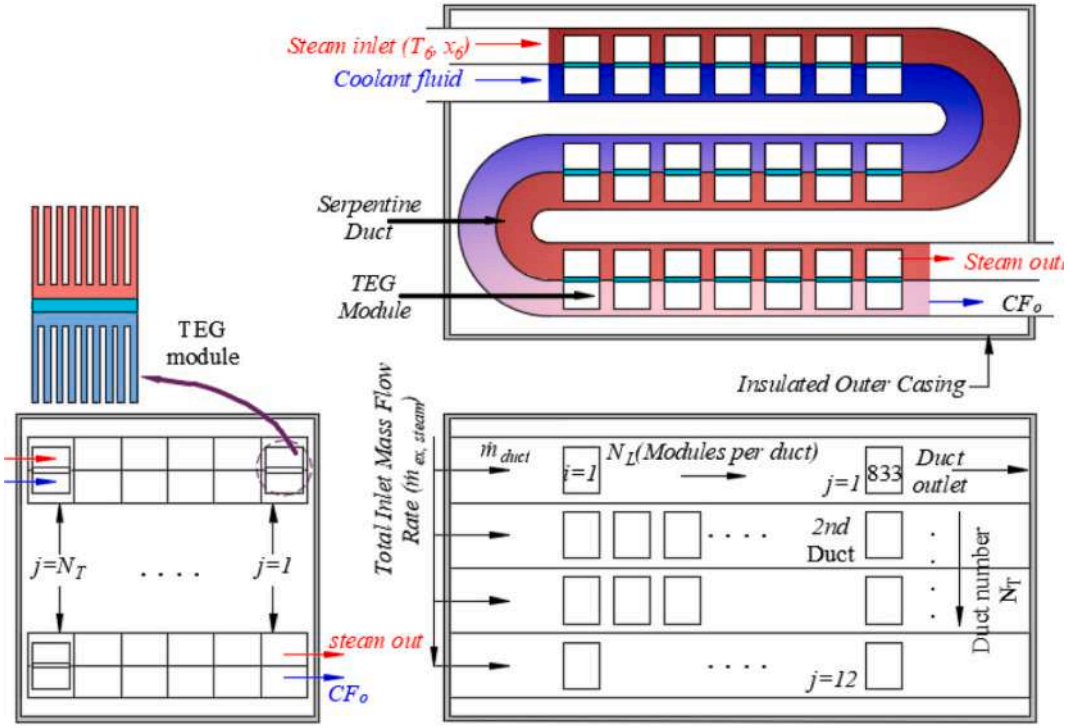

(a) Physical configuration showing the optimized serpentine duct arrangement

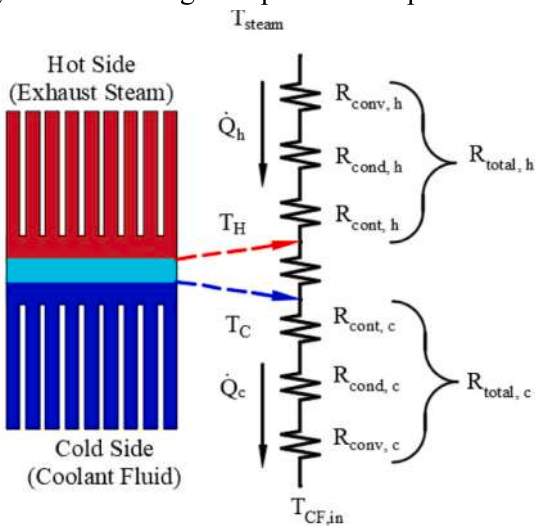

(b) One-dimensional TRN

Fig. 2. Schematic representation of the TEG subsystem.

present thermodynamic scope merit acknowledgment. The array's physical footprint, based on the 12 × 833 arrangement with each module occupying a 40 × 40 mm face area, corresponds to approximately 16 m^2 of active heat-transfer surface — a scale broadly consistent with industrial heat-exchanger installations already common in waste-heat-recovery facilities — though the full installed footprint, including duct casing, manifolding, and serviceability clearances, would be substantially larger. Electrical interconnection of 10,000 series/parallel-connected modules introduces wiring and bus-bar resistive losses not captured in the present per-module power calculation, and thermal contact resistance, modeled here as a single representative value per the TRN above, is expected to exhibit module-to-module variability in a manufactured array of this scale that could locally degrade performance below the idealized value used in the simulation. These considerations do not affect the validity of the thermodynamic cascade results presented in this study but identify manufacturability and electrical-interconnection losses as priorities for future experimental refinement.

2.3. HDH subsystem

The HDH stage produces freshwater using the low-quality steam (x_7) exiting the TEG. A Closed-Air-Open-Water (CAOW) configuration is adopted for its superior thermal efficiency over Closed-Water-Open-Air (CWOA) designs [56]. In HX-1, the waste steam pre-heats the incoming seawater feed in a counter-flow arrangement to the Top Brine Temperature. The thermally conditioned seawater is then sprayed over packing media in the Humidifier, evaporating into a recirculating air stream. The resulting saturated air passes through the Dehumidifier, where it is cooled by raw seawater, condensing vapor into high-purity distillate (State 16). The depleted steam exits HX-1 at State 8 and proceeds to the final recovery stage.

2.4. PEM electrolyzer subsystem

The PEM stage closes the energy and water loop. The exhaust stream (State 8) passes through HX-2, where its residual thermal energy pre-heats the HDH-produced distillate to the PEM optimal operating temperature of 80 °C — confirmed by thermodynamic analysis to be achievable without external electrical heating. The PEM electrolyzer stack then splits this preheated, high-purity water into hydrogen and oxygen using the combined DC power from the upstream ORC and TEG subsystems, ensuring that hydrogen production is driven entirely by recovered waste energy and waste-heat-purified water.

2.5. System state points

To ensure system reproducibility, Table 3 provides a comprehensive mapping of all numbered state points appearing in Fig. 1 to their corresponding fluid stream, location, representative operating temperature, pressure level, and thermodynamic phase or quality condition.

Table 3
Complete state-point definitions for Fig. 1.

State	Fluid	Location in System	T (°C)	P	Phase / Quality
1	ORC Fluid	Pump inlet	T_{cond}	P_{low}	Saturated liquid
2	ORC Fluid	Pump outlet / Evaporator inlet	$T_{cond} + \Delta T_{pump}$	P_{high}	Compressed liquid
3	ORC Fluid	Turbine inlet	*Tevap*	P_{high}	Sup. vapor / Trans.
4	ORC Fluid	Turbine outlet / Condenser inlet	T_{cond}	P_{low}	Wet or sup. Vapor
5	Waste Steam	System inlet	T_5=*90–200*	$P_{sat@T_5}$	x_5 = 0.8–1.0
6	Waste Steam	ORC evap. Outlet / TEG inlet	$T_{sat@x_6}$	P_{sat}	x_6 = 0.5 (fixed)
7	Waste Steam	TEG outlet / HX-1 inlet	$T_{sat@x_7}$	P_{sat}	x_7
8	Waste Steam	HX-1 outlet / HX-2 inlet	$T_{sat@x_8}$	P_{sat}	x_8 or liquid
9	Condensate	HX-2 outlet	$T_{WH,9}$	$P_{sat@T_{WH,9}}$	Liquid
10	Seawater	Raw seawater inlet	*25*	P_{atm}	Liquid
11	Seawater	HX-1 outlet / Humidifier inlet	T_{12}=*TBT*	P_{atm}	Liquid (heated)
12	Seawater	HX-1 seawater side inlet	*25*	P_{atm}	Liquid
13	Brine	Humidifier outlet	T_{13}		Liquid (reject)
14	Air	Humidifier inlet (dry)	T_{14}		Humid air
15	Air	Humidifier outlet	T_{15}	P_{atm}	Saturated humid air
16	Freshwater	Dehumidifier outlet	$T_{16,fresh}$	P_{atm}	Liquid distillate
17	Freshwater	HX-2 outlet / PEM inlet	*~80*	P_{atm}	Liquid (preheated)

3. Mathematical model analysis

A detailed mathematical model is required to simulate the behavior of the integrated system. To ensure transparency and reproducibility, Table 4 consolidates all key modeling assumptions adopted across the four subsystems. These assumptions are discussed in further detail within their respective subsection models.

A steam mass flow rate of $\dot{m}_{ex.steam}$= 5 kg/s is adopted as the system design basis. This value is representative of medium-scale industrial waste steam streams — such as those recovered from cement kilns, chemical reactors, and food processing facilities — and is consistent with mass flow rates employed in comparable WHR polygeneration studies in the literature [41,46].

To establish a unified and transparent simulation framework, all fixed operational parameters, component efficiencies, and geometric specifications across the integrated subsystems (ORC, TEG, HDH, and PEM) are consolidated in Table 5. These baseline values are extracted from established industrial standards and recent experimental literature to ensure the practical feasibility of the thermodynamic model.

3.1. Waste heat recovery model

The WHR system serves as the primary power plant, converting the latent heat in exhausted steam into electrical power. It is composed of the ORC and TEG subsystems arranged in a series thermodynamic cascade. The total net power generated by the WHR system ($\dot{W}_{net,WHR}$) is the sum of the net power from ORC ($\dot{W}_{net,ORC}$) and TEG ($\dot{W}_{net,TEG}$), as shown in Eq. (1):

$$\dot{W}_{net,WHR} = \dot{W}_{net,ORC} + \dot{W}_{net,TEG} \quad (1)$$

To solve Eq. (1), a thermodynamic model is developed independently for each power generation subsystem. The analysis begins with the first component in the cascade, the ORC subsystem.

3.1.1. ORC model

The ORC recovers the highest-grade portion of the steam's latent heat. The analysis follows standard Rankine cycle architecture (States 1–4). To establish the computational model, the following key assumptions and boundary conditions are made consistent with the assumptions summarized in Table 4. Firstly, the subsystem is designed to utilize the steam's latent heat until its quality drops to x_6 = 0.5, which defines the total heat input ($\dot{Q}_{in,ORC}$). Furthermore, component isentropic efficiencies are assumed to be 0.85 for the turbine, 0.80 for the pump, and 0.95 for the generator [29]. Finally, the ORC condenser is air-

Table 4
Consolidated modeling assumptions for the integrated poly-generation system.

#	Assumption	Subsystem	Ref
1	Steady-state operation throughout	All	
2	All working fluids treated as pure substances	All	
3	Pressure drops and heat losses in connecting pipes are negligible	All	
4	Changes in kinetic and potential energy are neglected	All	
5	ORC steam latent heat recovered until quality reaches $x_6 = 0.5$	ORC	
6	TEG p-n couples in electrical series and thermal parallel	TEG	[57]
7	TEG material properties are temperature-dependent	TEG	[58,59]
8	Heat dissipation from TEG external surfaces neglected	TEG	[60]
9	Complex fluid dynamics at the serpentine bends are simplified.	TEG	
10	A fixed external load resistance (R_{load}) is applied to each module.	TEG	
11	The two- phase pressure drop across the TEG array channels is considered negligible [a]		
12	The pumping power and fan power are considered minimal relative to the thermal energy input	HDH	[61,62]
13	Air and seawater treated as ideal mixtures in HDH	HDH	[63]
14	Top Brine Temperature constrained to 50–80 °C	HDH	[64]
15	The distillate water temperature (T_{16}) is approximated as the average of the dehumidifier inlet air dew point and the exit air dry-bulb temperature	HDH	[61]
16	PEM product gases (H_2, O_2) treated as ideal gases	PEM	
17	Membrane water content varies linearly across membrane thickness	PEM	[33]

[a] Verified quantitatively in Section 4.2 via two-phase pressure-drop analysis.

cooled, maintaining a constant condensing temperature of $40^{\circ}C$ [68].

The mathematical model employs a temperature-dependent control logic to optimize the operational regime (subcritical or transcritical) based on the relationship between the heat source temperature (T_5) and the critical temperature of the working fluid (T_{critical}).

When the heat source temperature permits evaporation below the fluid's critical points ($T_5 < T_{\text{critical}}$), the system operates in a subcritical mode. In this range, the high-side evaporation pressure (P_3) is governed by the Pinch Point Temperature Difference (ΔT_{PPTD}) at the evaporator, which represents the minimum temperature differential between the heat source and the working fluid, typically in the region of 10 K to 30 K [65,66]. For this study, the PPTD is set to 10 K, while the turbine inlet temperature (T_3) is determined by a Degree of Superheat (ΔT_{DSH}) of 5 K to ensure dry expansion [67]. These subcritical state relationships are expressed as:

$$T_{evap} = T_5 - \Delta T_{PPTD} \tag{2}$$

$$T_3 = T_{evap} + \Delta T_{DSH} \tag{3}$$

$$P_3 = P_{sat}(T_{evap}) < P_{critical} \tag{4}$$

Conversely, when the waste heat source temperature is sufficiently high to support supercritical operation (typically exceeding the fluid's critical temperature $T_5 \geq T_{\text{critical}}$), the system automatically transitions to transcritical mode. In this regime, instead of fixing the pressure, an adaptive pressure control strategy is implemented. The high-side pressure (P_3) is set to initiate slightly above the working fluid's critical pressure and increases linearly with the source temperature. This sliding-pressure strategy is crucial for minimizing the pump work penalty and ensuring a smooth transition without thermodynamic instabilities. Since no distinct phase change (boiling) occurs in the supercritical region, the turbine inlet temperature is defined by an Approach Point Temperature Difference (ΔT_{APTD}) of 10 K [66], as defined by:

Table 5
Fixed operational parameters and component specifications across all subsystems.

Parameter Description	Symbol	Value	Unit	Ref.
ORC Model				
Turbine Isentropic Efficiency	$\eta_{turbine}$	85	%	[29]
Pump Isentropic Efficiency	η_{pump}	80	%	[29]
Generator Efficiency	η_{gen}	95	%	[29]
Pinch Point Temperature Difference	ΔT_{PPTD}	10	K	[65,66]
Degree of Superheat	ΔT_{DSH}	5	K	[67]
Approach Point Temperature Difference	ΔT_{APTD}	10	K	[66]
Condensing Temperature	T_{cond}	40	°C	[68]
TEG Model				
Thermocouple (p-n) Count	n_{pn}	127	–	[54]
Module Dimensions	A_{TEG}	40 × 40	mm	[54]
Individual Leg Area	A_{leg}	1.4 × 1.4	mm	[54]
Duct Cross Section Area	A_{duct}	0.006	m^2	
Individual Leg length	L_{leg}	1.6	mm	[54]
Ceramic Plate thickness	t_{TEG}	0.8	mm	[54]
Total TEG height	H_{TEG}	3.9	mm	[54]
Total Number of Fins	n	19	–	[55]
Base Thermal Conductivity	k_b	235	W/m·K	[55]
Individual Fin dimension	$L_f \times t_f$	36 × 1.3	mm	[55]
Fin Spacing	d	0.9	mm	[55]
Base Dimension	A_b	41 × 40.5	mm	[55]
Base length	L_b	4	mm	[55]
External Load Resistance	R_{load}	3	Ω	
Coolant fluid inlet mass flow rate	$\dot{m}_{cf,i}$	25	Kg/s	
HDH Model				
Humidifier Effectiveness	ε_H	85	%	[69]
Dehumidifier Effectiveness	ε_D	85	%	[69]
Cycle Type	–	CAOW	–	[56]
Exit Relative Humidity	ϕ_{out}	100	%	[70]
Seawater Salinity	–	35	g/kg	[63]
PEM Electrolyzer Model				
Stack Temperature	T_{PEM}	80	°C	[4]
Cell Active Area	A_{cell}	0.0877	m^2	[71]
Cells in Series	N_{stack}	300	–	[71]
Membrane Thickness	L	50	μm	[72,73]

$$P_3 = f(T_5) > P_{critical} \tag{5}$$

$$T_3 = T_5 - \Delta T_{APTD} \tag{6}$$

While R245fa ($T_{\text{critical}} \approx 154^{\circ}C$), serves as the baseline fluid, the computational model incorporates a comparative parametric study evaluating alternative fluids—n-Pentane ($T_{\text{critical}} \approx 196.5^{\circ}C$) and Cyclopentane ($T_{\text{critical}} \approx 238^{\circ}C$) —to assess their potential in optimizing system stability across the varying operational range.

The heat absorbed by the ORC evaporator ($\dot{Q}_{in,ORC}$), is calculated from the enthalpy drop of the steam:

$$\dot{Q}_{in,ORC} = \dot{m}_{ex.steam} \bullet (h_5 - h_6) \tag{7}$$

where *h*is the specific enthalpy of the steam as a function of temperature and steam quality.

The pump pressurizes the liquid organic fluid to the high-side pressure (P_3). The actual specific pump work (W_p) and enthalpy (h_2) are calculated using the pump's isentropic efficiency (η_{pump}):

$$W_p = \frac{h_{2s} - h_1}{\eta_{pump}} \tag{8}$$

$$h_2 = W_p + h_1 \tag{9}$$

where is h_{2s} is the isentropic enthalpy at the pump outlet

The actual specific work generated by the turbine (W_t) and the actual enthalpy (h_4) are found using the turbine's isentropic efficiency ($\eta_{turbine}$):

$$W_t = \eta_{turbine} \bullet (h_3 - h_{4s}) \tag{10}$$

$$h_4 = h_3 - W_t \tag{11}$$

where h_{4s} is the isentropic enthalpy at the turbine outlet

The mass flow rate of the ORC working fluid ($\dot{m}_{ORC}$) is calculated by balancing the heat input from exhausted steam:

$$\dot{m}_{ORC} = \frac{\dot{Q}_{in,ORC}}{h_3 - h_2} \tag{12}$$

The net electrical power generated by the ORC ($\dot{W}_{net,ORC}$) is the generator-adjusted turbine power minus the pump power:

$$\dot{W}_{net,ORC} = (\dot{m}_{ORC} \bullet W_t \bullet \eta_{gen}) - (\dot{m}_{ORC} \bullet W_p) \tag{13}$$

where η_{gen} is the generator efficiency

Finally, the thermal efficiency of the ORC subsystem is:

$$\eta_{th,ORC} = \frac{\dot{W}_{net,ORC}}{\dot{Q}_{in,ORC}} \tag{14}$$

3.1.2. TEG model

The TEG subsystem recovers the "second portion" of the steam's latent heat (wet steam at x_6, T_6). The model utilizes a coupled thermo-electrical energy balance. The mathematical formulation of the TEG subsystem model is based on the following foundational assumptions governed by the assumptions listed in Table 4. Notably, the 833 sequential modules per duct are assumed to impose a negligible pressure drop on the steam flow (Table 4).

To verify the validity of the negligible-pressure-drop assumption adopted in the TEG thermal model, a dedicated two-phase frictional pressure-drop analysis was performed for the 833-module serpentine duct geometry. Each parallel duct has a rectangular cross-section area (A_{duct}) and carries a per-duct steam mass flow rate ($\dot{m}_{ex,steam,duct}$). The frictional pressure drop was estimated using the classical Darcy–Weisbach relation for the liquid-only and vapor-only flow components:

$$\Delta P_{LO} = f_{LO} \frac{L}{D_h} \frac{{G_m}^2}{2\rho_f} \tag{15}$$

$$\Delta P_{GO} = f_{GO} \frac{L}{D_h} \frac{{G_m}^2}{2\rho_g} \tag{16}$$

where ΔP_{LO} and ΔP_{GO} are the pressure drops that would occur if the liquid or vapor phase, respectively, flowed alone through the duct at the total mass flux; L is the total duct length; D_h is the hydraulic diameter; G_m is the total mass flux (mass flow rate per unit cross-sectional area); and ρ_f and ρ_g are the saturated liquid and vapor densities at the local saturation pressure.

The corresponding Darcy friction factors (f_{LO} and f_{GO}), evaluated using the turbulent smooth-tube correlation [74]:

$$f = 0.184 \bullet Re^{-0.2} \tag{17}$$

The two single-phase pressure drops were then combined using the separated-flow framework of Lockhart and Martinelli, in which the Martinelli parameter X is defined as [75]:

$$X = \sqrt{\frac{\Delta P_{LO}}{\Delta P_{GO}}} \tag{18}$$

The resulting two-phase frictional pressure drop is obtained through the Chisholm two-phase multiplier [76]:

$$\phi_L^2 = 1 + \frac{C}{X} + \frac{1}{X^2} \tag{19}$$

$$\Delta P_{two-phase} = \phi_L^2 \, \Delta P_{LO} \tag{20}$$

where ϕ_L^2 is the two-phase frictional multiplier applied to the liquid-only pressure drop, and C is an empirical constant that depends on the flow regime of each phase; for turbulent–turbulent flow, the value $C = 20$ [76].

To assess the thermal significance of the resulting pressure drop, the corresponding shift in the local saturation temperature was estimated using the Clausius–Clapeyron relation [77]:

$$\frac{dT_{sat}}{dP} = \frac{T_{sat} v_{fg}}{h_{fg}} \tag{21}$$

where T_{sat} is the saturation temperature in Kelvin, v_{fg} is the specific volume difference between the saturated vapor and saturated liquid phases, and h_{fg} is the latent heat of vaporization at the local saturation pressure.

Based on these assumptions, the model is constructed by applying a couple of thermo-electrical energy balances. The analysis begins with the core equations governing the performance of a single module. The Seebeck coefficient (α_p, α_n), thermal conductivities (K_p, K_n), and electrical resistivities (ρ_p, ρ_n) for the p-type and n-type legs are calculated using polynomial correlations derived from experimental data [58].

$$\alpha_{p(T)} = \left[5.921 \bullet 10^{-13} \bullet T^3 - 3.274 \bullet 10^{-9} \bullet T^2 + 2.422 \bullet 10^{-6} \bullet T - 2.744 \bullet 10^{-4}\right] \tag{22}$$

$$\alpha_{n(T)} = \left[1.292 \bullet 10^{-13} \bullet T^3 + 1.074 \bullet 10^{-9} \bullet T^2 - 9.272 \bullet 10^{-7} \bullet T + 8.959 \bullet 10^{-6}\right] \tag{23}$$

$$\rho_{p(T)} = \left[2.249 \bullet 10^{-14} \bullet T^3 - 1.251 \bullet 10^{-10} \bullet T^2 + 1.389 \bullet 10^{-7} \bullet T - 2.245 \bullet 10^{-5}\right] \tag{24}$$

$$\rho_{n(T)} = \left[-1.246 \bullet 10^{-14} \bullet T^3 - 6.429 \bullet 10^{-11} \bullet T^2 + 9.103 \bullet 10^{-8} \bullet T - 1.049 \bullet 10^{-5}\right] \tag{25}$$

$$K_{p(T)} = \left[1.252 \bullet 10^{-7} \bullet T^3 - 1.243 \bullet 10^{-4} \bullet T^2 + 3.874 \bullet 10^{-2} \bullet T - 2.363\right] \tag{26}$$

$$K_{n(T)} = \left[-1.593 \bullet 10^{-8} \bullet T^3 + 2.906 \bullet 10^{-5} \bullet T^2 - 1.583 \bullet 10^{-2} \bullet T + 3.728\right] \tag{27}$$

The individual leg properties are aggregated into equivalent junction parameters representing a single p-n thermocouple pair [78].

$$\alpha_{pn\ (T)} = \alpha_{p(T)} - \alpha_{n(T)} \tag{28}$$

$$K_{pn(T)} = \frac{(K_{p(T)} + K_{n(T)}) \bullet A_{leg}}{L_{leg}} \tag{29}$$

$$R_{pn(T)} = \frac{(\rho_{p(T)} + \rho_{n(T)}) \bullet L_{leg}}{A_{leg}} \tag{30}$$

where A_{leg} (m^2) and L_{leg} (m) are the cross-sectional area and length of each semiconductor leg, respectively.

The heat absorbed at the hot side and rejected at the cold side of a single p-n couple are governed by Peltier heat, Fourier conduction, and Joule heating [79]:

$$\dot{Q}_h = n_{pn} \bullet \left[\alpha_{pn(T)} \bullet I \bullet T_h + K_{pn(T)} \bullet (T_h - T_c) - 0.5 \bullet I^2 \bullet R_{pn(T)}\right] \tag{31}$$

$$\dot{Q}_c = n_{pn} \bullet \left[\alpha_{pn(T)} \bullet I \bullet T_c + K_{pn(T)} \bullet (T_h - T_c) + 0.5 \bullet I^2 \bullet R_{pn(T)}\right] \tag{32}$$

where I is the electric current, T_h and T_c are the hot and cold surface temperatures, respectively, and R_{pn} is the electrical resistance of a single pn couple (Ω).

The electric current and module power output follow directly from these properties:

$$I = \frac{\alpha_{pn(T)} \cdot (T_h - T_c)}{R_{pn(T)} + R_{load}} \tag{33}$$

$$P_{module} = I^2 \bullet R_{load} \tag{34}$$

Because the material properties in Eqs. (15)–(20) depend on the module surface temperatures, which are themselves unknown, the system is nonlinear and coupled. To close it, the module surface temperatures ($T_h$and T_c) are linked to the known bulk fluid temperatures via a TRN, illustrated in Fig. 2a. On each side, heat traverses three resistances in series: a convective resistance at the fin surface (R_{conv}), a conductive resistance through the heat sink base (R_{cond}), and a contact resistance at the ceramic interface (R_{cont}) [80,81]:

$$R_{th,total} = R_{contact} + R_b + R_{conv} \tag{35}$$

$$R_{contact} = \frac{R''_{t,c}}{A_b} \tag{36}$$

$$R_b = \frac{L_b}{k_b \bullet A_b} \tag{37}$$

$$R_{conv} = \frac{1}{h_{conv} \bullet A_{eff}} \tag{38}$$

where $R''_{t,c}$ is the specific thermal contact resistance (2.5×10^{-6} m^2.K/W [82]), L_b and k_b are the base thickness (m) and thermal conductivity (W/m·K), and $A_b$is the base area ($A_b = W_b \bullet L_b$).

The effective heat transfer area (A_{eff}) accounts for fin efficiency, and is evaluated as [82]:

$$A_{eff} = A_{b,unfinned} + (A_{f,total} \bullet \eta_f) \tag{39}$$

where η_f is the fin efficiency, assuming an adiabatic fin tip, defined as:

$$\eta_f = \frac{\tanh m \bullet L_f}{m \bullet L_f} \tag{40}$$

where m is the fin parameter, defined as:

$$m = \sqrt{\frac{2h_{conv}}{k_f \bullet t_f}} \tag{41}$$

The total surface area of the fins ($A_{f,total}$) and the exposed unfinned base area ($A_{b,unfinned}$) are geometrically determined by:

$$A_{f,total} = 2 \bullet n_f \bullet L_f \bullet W_b \tag{42}$$

$$A_{b,\text{unfinned}} = A_b - (n_f \bullet t_f \bullet W_b) \tag{43}$$

where W_b is the width of the heat sink base into the flow direction, A_b is the total footprint area of the heat sink base ($A_b = W_b \bullet L_b$), and k_f is the base/ fin thermal conductivity.

The convective coefficient (h_{conv}) on the hot side (two-phase condensing steam) is calculated using the Shah correlation [83]. To apply this correlation, the mass flux (G_m) is first determined from the duct geometry and per-duct mass flow rate:

$$G_m = \frac{\dot{m}_{ex,steam,duct}}{A_{duct}} \tag{44}$$

The liquid-phase heat transfer coefficient (h_l) and vapor quality correction factor (Z) are [11]:

$$h_l = 0.023 \bullet \frac{k_l}{D_h} \bullet \left[\frac{G_m \bullet (1-x) \bullet D_h}{\mu_l}\right]^{0.8} \bullet \mathrm{Pr}_l^{0.4} \tag{45}$$

$$Z = \left[\frac{1-x}{x}\right]^{0.8} \bullet P_r^{0.4} \tag{46}$$

The total hot-side convective coefficient is then:

$$h_{conv,h} = h_l \bullet \left[1 + \frac{3.8}{Z^{0.95}}\right] \tag{47}$$

where G_m is the mass velocity (kg/m^2. s), A_{duct} is the cross-sectional flow area of a single duct (m^2), P_r is the reduced pressure, defined as the ratio of the steam's saturation pressure to its critical pressure, and x is the local vapor quality of the steam at a given cross-section along the duct.

On the cold side, the coolant fluid flows as a single phase and absorbs waste heat from the system. Since the coolant fluid is actively being heated during this process, the convective heat transfer coefficient ($h_{conv,c}$) is calculated using the standard Dittus-Boelter correlation with a Prandtl number exponent of 0.4. The correlation is valid for fully developed turbulent flow ($Re \geq 10,000$) and $0.7 \leq \mathrm{Pr} \leq 160$ [81], which aligns with the operating conditions of the coolant channel.

$$Nu_c = 0.023 \bullet Re^{0.8} \bullet \mathrm{Pr}^{0.4} \tag{48}$$

$$h_{conv,c} = \frac{Nu \bullet k_{cf}}{D_h} \tag{49}$$

The heat fluxes from the fluid to the module surfaces are then:

$$\dot{Q}_{h,conv} = \frac{T_5 - T_h}{R_{th,total,h}} \tag{50}$$

$$\dot{Q}_{c,conv} = \frac{T_c - T_{cf}}{R_{th,total,c}} \tag{51}$$

This establishes a system of three non-linear equations that are solved simultaneously for the three unknowns (T_h, T_c, I) at each control volume step (i):

$$\dot{Q}_h(T_h, T_h, I) - \dot{Q}_{h,conv}(T_h) = 0 \tag{52}$$

$$\dot{Q}_c(T_h, T_h, I) - \dot{Q}_{c,conv}(T_h) = 0 \tag{53}$$

$$(\dot{Q}_h - \dot{Q}_c) - (I^2 \bullet R_{load}) = 0 \tag{54}$$

Since the model is discretized into 833 sequential control volumes, the outlet conditions of each (i) define the inlet conditions for the module ($i+1$).

Based on the calculated heat transfer ($\dot{Q}_h, \dot{Q}_c$), the fluid properties are updated using the energy conservation principle: For the steam (hot side), the specific enthalpy drops due to heat extraction.

$$h_{steam,out,i} = h_{steam,in,i} - \frac{\dot{Q}_{h,i}}{\dot{m}_{ex,steam,duct}} \tag{55}$$

The new steam quality is then updated.

$$x_{,out,i} = \frac{h_{steam,out,i} - h_f}{h_g - h_f} \tag{56}$$

where h_f, and h_g are the specific enthalpies of saturated liquid and saturated vapor, respectively, evaluated at the steam saturation temperature.

For the cooling fluid on the cold side, the temperature increases:

$$T_{cf,out,i} = T_{cf,in,i} + \frac{\dot{Q}_{c,i}}{\dot{m}_{cf,i,duct} \bullet C_{p,cf}} \tag{57}$$

where $C_{p,cf}$ is the specific heat capacity of the cooling fluid at constant pressure.

The cumulative power of the TEG subsystem is the summation of the power generated by all modules (N_{total}) across all ducts:

$$\dot{W}_{net,TEG} = \sum_{i=1}^{N_{total}} P_{module,i} \tag{58}$$

Finally, the TEG efficiency is defined as:

$$\eta_{net,TEG} = \frac{\dot{W}_{net,TEG}}{\dot{Q}_{in,TEG}} \tag{59}$$

where $\dot{Q}_{in,TEG}$ is the total heat absorbed by the TEG module

Since the model is discretized, this value is calculated as the summation of the heat absorbed by the hot side of each module (i) across all 12 ducts:

$$\dot{Q}_{in,TEG} = 12 \bullet \sum_{i=1}^{833} \dot{Q}_{h,i} \tag{60}$$

To solve the discretized coupled system described above, specific geometric dimensions and material properties are required. Table 5 details the technical specifications for both the commercial thermoelectric modules and the aluminum plate-fin heat sinks adopted in this simulation.

Several simplifying assumptions in the TEG thermal-electrical model warrant explicit discussion regarding their expected influence on predicted power output. Bend-induced secondary flow, neglected in treating each of the 833 control volumes as an equivalent straight-duct segment, simultaneously enhances local heat transfer and increases pressure losses; its net effect on TEG power is therefore of uncertain sign but expected to remain second-order relative to the dominant two-phase resistance already resolved at each step.

The fixed external load resistance (R_{load}= 3 Ω), applied uniformly despite the internal resistance varying with local module temperature, causes the array to operate away from its temperature-dependent maximum-power-point, making the reported power a conservative estimate relative to an idealized maximum-power-point-tracked array. Neglected casing heat loss to ambient similarly biases the reported power toward a mild overestimate, while linearly scaling the single validated module (Section 4.1) to the full 10,000-module array, without accounting for manufacturing tolerances or contact-resistance variability, introduces a comparable optimistic bias. These four simplifications should therefore be read as bounding the reported TEG power as a representative first-order estimate, with prototype-scale validation identified as a priority for future work.

3.2. HDH model

The HDH unit recovers the remaining latent heat (x_7), for freshwater production.

CAOW configuration is utilized. The mathematical formulation of the HDH system model is based on the following foundational assumptions, as outlined in Table 4. Based on these assumptions, the mathematical model is formulated using the mass and energy conservation laws for the primary components: the dehumidifier, the humidifier, and the seawater heat exchanger. The governing heat and mass transfer equations are consolidated in Table 6.

In the HDH model, component effectiveness is evaluated against thermodynamic limits. Specifically, the ideal air enthalpy assumes the air reaches full saturation at the seawater inlet temperature, while the ideal seawater enthalpy assumes the water temperature reaches the inlet air's dry-bulb temperature. To evaluate the performance indicators defined above, the model incorporates specific operational constraints and component characteristics. The fixed HDH operational parameters are summarized in Table 5.

3.3. PEM Electrolyzer model

The final subsystem converts the recovered electrical power ($\dot{W}_{PEM}$) and high-purity water ($\dot{m}_{16,fresh}$) into green hydrogen, simultaneously closing the thermal loop.

The mathematical modeling of this subsystem is established under steady-state as outlined in Table 4, and product gases (H_2,O_2) are treated as ideal gases. Furthermore, the membrane water content (λ) is assumed to vary linearly across the membrane thickness to simplify the analysis of transport phenomena.

The thermodynamic identity governs the total energy required to split water into hydrogen and oxygen [43,72,87]:

$$\Delta H = \Delta G + T_{PEM}\Delta S \tag{72}$$

where ΔH is the total enthalpy of reaction, ΔG is the Gibbs free energy that must be supplied electrically, and $T_{PEM}\Delta S$ is the thermal energy contribution.

By operating at an elevated temperature of 80 °C, the thermal term $T_{PEM}\Delta S$ increases, effectively reducing the electrical demand ΔG— the primary motivation for integrating waste heat pre-heating with the PEM electrolyzer. The minimum thermodynamic voltage required to initiate water splitting is the reversible potential V_0, which decreases with increasing temperature according to the Nernst equation [87]:

Table 6
Governing mass and energy balances and performance metrics for the HDH subsystem [84–86].

	Governing Equation	Eq.
Dehumidifier		
Mass	$\dot{m}_{16,fresh} = \dot{m}_{air} \bullet (\omega_{air,15} - \omega_{air,14})$	(61)
Energy	$\dot{m}_{air} \bullet (h_{air,15} - h_{air,14}) = \dot{m}_{10,sw} \bullet (h_{11} - h_{10}) + \dot{m}_{16,fresh} \bullet h_{16}$	(62)
Effectiveness	$\varepsilon_D = max\left[\frac{(h_{15} - h_{14})}{(h_{15} - h_{14,ideal})}, \frac{(h_{11} - h_{10})}{(h_{11,ideal} - h_{10})}\right]$	(63)
Humidifier		
Mass	$\dot{m}_{13,brine} = \dot{m}_{10,sw} - \dot{m}_{16,fresh}$	(64)
Energy	$\dot{m}_{10,sw} \bullet h_{12} - \dot{m}_{13,brine} \bullet h_{13} = \dot{m}_{air} \bullet (h_{15} - h_{14})$	(65)
Effectiveness	$\varepsilon_H = max\left[\frac{(h_{15} - h_{14})}{(h_{15,ideal} - h_{14})}, \frac{(h_{12} - h_{13})}{(h_{12} - h_{13,ideal})}\right]$	(66)
HX-1		
Heat Input	$\dot{Q}_{req,HDH} = \dot{m}_{10,sw} \bullet (h_{12} - h_{11})$	(67)
	$h_8 = h_7 - \frac{\dot{Q}_{req,HDH}}{\dot{m}_{ex,steam}}$	(68)
HDH Performance		
GOR	$GOR = \frac{\dot{m}_{16,fresh} \bullet h_{fg}}{\dot{Q}_{req,HDH}}$	(69)
RR	$RR = \frac{\dot{m}_{16,fresh}}{\dot{m}_{10,sw}}$	(70)
MR	$MR = \frac{\dot{m}_{10,sw}}{\dot{m}_{air}}$	(71)

$$V_0 = 1.229 - 8.5 \times 10^{-4} \bullet (T_{PEM} - 298) \tag{73}$$

where T_{PEM} is in *Kelvin (K)*

To drive the reaction at a practical rate, additional voltages (overpotentials) must be overcome. The exchange current density quantifies the intrinsic electrochemical activity of each electrode $J_{0,i}$, which follows an Arrhenius-type dependence on temperature [43,87,88]:

$$J_{0,i} = J_i^{ref} \bullet \exp\left(-\frac{E_{act,i}}{R \bullet T_{PEM}}\right) \; i = anode, cathode \tag{74}$$

where J_i^{ref} is the reference exchange current density (A/m^2), $E_{act,i}$ is the activation energy (J/mol), and R is the universal gas constant (J/mol. K).

The voltage required to overcome the kinetic energy barrier at each electrode surface is modeled using the Butler-Volmer equation [43,72,87]:

$$V_{act,i} = \frac{RT_{PEM}}{F} sinh^{-1}\left(\frac{J}{2J_{0,i}}\right) \; \mathrm{i} = anode, cathode \tag{75}$$

where $F = 96,485$ C/mol is Faraday's constant and J is the operating current density (A/m^2).

Furthermore, ohmic losses arise from the membrane's resistance to proton transport. The average ionic conductivity ($\bar{\sigma}_{PEM}$) of the membrane is evaluated at the mean water content ($\bar{\lambda}$) [43]:

$$\bar{\sigma}_{PEM} = \left(0.5139\bar{\lambda} - 0.326\right) exp\left[1268 \bullet \left(\frac{1}{303} - \frac{1}{T_{PEM}}\right)\right] \tag{76}$$

where $\bar{\sigma}_{PEM}$ is the average ionic conductivity in S/m.

The membrane resistance (R_{PEM}) and the corresponding ohmic overpotential (V_{ohm}) are then [89]:

$$R_{PEM} = \frac{L}{\sigma_{PEM}} \tag{77}$$

$$V_{ohm} = J \bullet R_{PEM} \tag{78}$$

where L is the membrane thickness (m).

Finally, the operational cell voltage (V_{cell}) is the sum of the reversible potential and the irreversible overpotentials [43,90]:

$$V_{cell} = V_0 + V_{\mathrm{act,anode}} + V_{\mathrm{act,cathode}} + V_{\mathrm{ohm}} \tag{79}$$

Since V_{cell} is a nonlinear function of the current density ($J = I_{stack}/A_{cell}$), the total stack power balance ($\dot{W}_{PEM}$) is expressed as:

$$\dot{W}_{PEM} = N_{cells} \bullet V_{cell} \bullet I_{stack} \tag{80}$$

Once the operating current I_{stacks} is resolved for the available power input $\dot{W}_{PEM}$, the molar hydrogen production rate ($\dot{N}_{H_2,out}$) is governed by Faraday's law [72]:

$$\dot{N}_{H_2,out} = \frac{N_{cells} \bullet I_{stacks}}{2F} \tag{81}$$

The stoichiometric oxygen production rate ($\dot{N}_{\mathrm{O_2,out}}$) and the residual water flow ($\dot{N}_{H_2O,out}$) are determined by mass balances:

$$\dot{N}_{\mathrm{O_2,out}} = \frac{1}{2}\dot{N}_{H_2,out} \tag{82}$$

$$\dot{N}_{H_2O,out} = \dot{N}_{H_2O,in} - \dot{N}_{H_2,out} \tag{83}$$

The PEM subsystem efficiency is evaluated on a Higher Heating Value (HHV) basis, as the feedwater enters the stack as a liquid and the total energy content of the produced hydrogen — including the latent heat of vaporization — is relevant to the system energy balance [91,92]:

$$\eta_{PEM} = \frac{\dot{m}_{H_2,out} \bullet HHV_{H2}}{\dot{W}_{PEM}} \tag{84}$$

where $HHV_{H_2} \approx 141.8$MJ/kg.

The activation energy barriers and exchange current factors specific to each electrode are detailed in Table 7. and exergy balance equations are detailed in Table 8.

3.4. Overall system performance

To evaluate the thermodynamic performance of the fully integrated system, two distinct parameters are defined to differentiate between high-grade energy conversion and total resource utilization.

First, the overall system efficiency (η_{sys}) assesses the conversion of low-grade waste heat into high-value hydrogen energy.

$$\eta_{sys} = \frac{\dot{m}_{H_2,out} \bullet HHV_{H2}}{\dot{Q}_{in,total}} \tag{85}$$

The Higher Heating Value (HHV = 141.8 MJ/kg) is selected as the efficiency reference because the PEM electrolyzer operates with liquid water feedstock at a low temperature (80 °C). Unlike combustion systems where latent heat is lost via water vapor in exhaust streams, low-temperature electrolytic systems preserve the chemical potential for full latent heat recovery, making HHV the thermodynamically correct reference for total stored energy. Adopting the Lower Heating Value (LHV = 120 MJ/kg) would artificially inflate the reported efficiency by 18.2% (HHV/LHV = 1.182), misrepresenting the system performance. This approach strictly aligns with standard evaluation metrics in liquid-fed electrolysis literature [72,87].

Second, to account for the simultaneous production of freshwater, which represents a significant portion of the recovered thermal energy, the EUF is introduced. This metric represents the ratio of all useful outputs (Hydrogen energy + Latent heat of the net freshwater surplus) to the total thermal energy extracted from the waste source ($\dot{Q}_{in,total}$).

$$EUF = \frac{\left(\dot{m}_{H_2,out} \bullet HHV_{H2}\right) + \left(\dot{m}_{16,fresh} - \dot{m}_{\mathrm{H2O,cons}}\right) \bullet h_{fg}}{\dot{Q}_{in,total}} \tag{86}$$

where $\dot{m}_{H_2,out}$ and $\dot{m}_{\mathrm{H2O,cons}}$ are the hydrogen production and water consumption rates calculated in the PEM model.

3.5. Exergy analysis model

To complement the first law (energy-based) evaluation, a complete second law (exergy) analysis is developed to quantify the thermodynamic irreversibilities within each subsystem and identify the components responsible for the degradation of available work potential across the cascade. The exergy analysis is performed with respect to a reference (dead) state defined as $T_0 = 298.15$ K (25 °C) and $P_0 = 101.325$ kPa. For any single-phase or two-phase pure-substance stream at state i neglecting kinetic and potential exergy, the specific physical exergy is:

$$ex_i = (h_i - h_0) - T_0(s_i - s_0) \tag{87}$$

Table 7
Key design specifications for the PEM electrolyzer model.

System Parameter	Symbol	Anode Value	Cathode value	Unit	Ref.
Activation Energy Barrier	E_{act}	76	18	kJ/mol	[72,73]
Exchange Current Factor	J^{ref}	1.764×10^5	4.61×10^5	A/m^2	
Water Content Interface	λ	14	10	–	
Electrolyte Thickness	L	50	–	μm	

Table 8
Summary of exergy balance equations used in the integrated ORC–TEG–HDH–PEM system.

Component	Exergy balance equation	
ORC subsystem		
Evaporator	$\dot{E}x_{dest,evap} = \dot{m}_{ex,steam}(ex_5 - ex_6) - \dot{m}_{wf}(ex_3 - ex_2)$	(89)
Turbine	$\dot{E}x_{dest,turb} = \dot{m}_{ORC}(ex_3 - ex_4) - \dot{W}_{T,actual}$	(90)
Condenser	$\dot{E}x_{dest,cond} = \dot{m}_{ORC}(ex_4 - ex_1) - \dot{Q}_{cond}\left(1\frac{T_0}{T_{cond}}\right)$	(91)
Pump	$\dot{E}x_{dest,pump} = \dot{W}_{P,actual} - \dot{m}_{ORC}(ex_2 - ex_1)$	(92)
TEG subsystem		
	$\dot{E}x_{dest,TEG} = \dot{m}_{ex,steam}(ex_6 - ex_7) - \dot{W}_{net,TEG}$	(93)
HDH Subsystem		
HX-1	$\dot{E}x_{dest,HX1} = \dot{m}_{ex,steam}(ex_7 - ex_8) - \dot{m}_{10,sw}(ex_{11} - ex_{10})$	(94)
Humidifier	$\dot{E}x_{dest,hum} = \dot{m}_{10,sw}ex_{11} - \dot{m}_{13,brine}ex_{13} - \dot{m}_{air}(ex_{15} - ex_{14})$	(95)
Dehumidifier	$\dot{E}x_{dest,dehum} = \dot{m}_{air}(ex_{15} - ex_{14}) - \dot{m}_{16,fresh}ex_{16}$	(96)
PEM Subsystem		
HX-2	$\dot{E}x_{dest,HX2} = \dot{m}_{ex,steam}(ex_8 - ex_9) - \dot{m}_{16,fresh}(ex_{17} - ex_{16})$	(97)
PEM stack	$\dot{E}x_{dest,PEM} = \dot{W}_{PEM} + \dot{m}_{w,in}ex_{17} - \dot{m}_{H_2}ex_{H_2}$	(98)

where h_i and s_i are the specific enthalpy (kJ/kg) and specific entropy (kJ/kg. K) of the stream at its actual state, and h_0 and s_0 are the corresponding properties evaluated at the dead state (T_0, P_0). The total exergy rate of a stream of mass flow rate $\dot{m}_i$ is

$$\dot{E}x_i = \dot{m}_i \cdot ex_i \tag{88}$$

The exergy destruction rates for the individual components of the ORC, TEG, HDH, and PEM subsystems are formulated based on the general exergy balance equation ($\dot{E}x_{in} = \dot{E}x_{out} + \dot{E}x_{dest} + \dot{W}$) and are summarized in Table 8.

The total exergy destruction across the integrated cascade is the sum of all subsystem contributions:

$$\dot{E}x_{dest,total} = \dot{E}x_{dest,ORC} + \dot{E}x_{dest,TEG} + \dot{E}x_{dest,HDH} + \dot{E}x_{dest,HX2} + \dot{E}x_{dest,PEM} \tag{99}$$

The total exergy input to the system is the physical exergy of the incoming waste steam relative to the dead state:

$$\dot{E}x_{in,total} = \dot{m}_{ex,steam} \cdot ex_5 \tag{100}$$

System-wide exergy balance closure is verified by:

$$\dot{E}x_{in,total} = \dot{E}x_{dest,total} + \dot{m}_{H_2}ex_{H_2} + \dot{m}_{ex,steam}ex_9 \tag{101}$$

The final term represents the residual physical exergy retained in the spent steam exiting HX-2 (State9), which is not recovered by the present cascade architecture.

The exergetic efficiency of each subsystem is defined as the ratio of exergy in the desired product to the supplied exergy:

$$\psi_{ORC} = \frac{\dot{W}_{net,ORC}}{\dot{m}_{ex,steam}(ex_5 - ex_6)} \tag{102}$$

$$\psi_{TEG} = \frac{\dot{W}_{net,TEG}}{\dot{m}_{ex,steam}(ex_6 - ex_7)} \tag{103}$$

$$\psi_{HDH} = \frac{\dot{m}_{16,fresh}ex_{16}}{\dot{m}_{ex,steam}(ex_7 - ex_8)} \tag{104}$$

$$\psi_{PEM} = \frac{\dot{m}_{H_2}ex_{H_2}}{\dot{W}_{PEM} + \dot{m}_{w,in}ex_{17}} \tag{105}$$

The overall system exergetic efficiency, expressing the fraction of the incoming steam's exergy ultimately converted into the chemical exergy of the hydrogen product, is:

$$\psi_{sys} = \frac{\dot{m}_{H_2}ex_{H_2}}{\dot{E}x_{in,total}} \tag{106}$$

3.6. Economic and environmental assessment framework

3.6.1. Economic analysis

To assess commercial viability, a techno-economic model is developed that converts physical sizing parameters—obtained from the thermodynamic simulation—into capital (CAPEX) and operational (OPEX) expenditures. The system is designed as a hydrogen production facility in which electricity and freshwater are consumed internally by the PEM electrolyzer, yielding green hydrogen as the sole commercial product.

The total capital expenditure (CAPEX) aggregates the purchased equipment costs (Z_k) with a 15% miscellaneous factor (f_{misc}) to account for installation and piping:

$$CAPEX_{total} = (1 + f_{misc})\sum Z_k \tag{107}$$

The annual OPEX is estimated at 4% of CAPEX, covering maintenance and auxiliary costs. Component cost functions (Z_k) are detailed in Table 9.

Profitability is evaluated using three indicators: NPV, LCOH, and PBP. These are calculated over a project lifetime of 20 years (N) at a 10% discount rate (r), using the Capital Recovery Factor (CRF) [97,98]:

$$CRF = \frac{r(1+r)^N}{(1+r)^N - 1} \tag{108}$$

LCOH represents the minimum price required to recover all life-cycle costs:

$$LCOH = \frac{CAPEX_{total} \cdot CRF + OPEX_{total}}{\dot{M}_{H2} \cdot t_{op}} \tag{109}$$

The NPV quantifies the project's absolute economic value by discounting all future net cash flows to the present. A positive NPV confirms commercial viability at the specified discount rate [99]:

$$NPV = -CAPEX_{total} + \sum_{n=1}^{N} \frac{Revenue_{annual} - OPEX_{total}}{(1+r)^n} \tag{110}$$

$$Revenue_{annual} = \dot{M}_{H2} \cdot t_{op} \cdot P_{H2} \tag{111}$$

where P_{H2} is the market price of hydrogen 5 USD/kg [100–102]

The PBP determines the number of years required for cumulative net operating profit to recover the initial capital:

Table 9
Equipment capital cost functions.

Subsystem	Component	Cost Function (Z_k) [USD]	Ref.
TEG	Module array	$Z_{TEG} = 1500 \bullet \dot{W}_{net,TEG}$	[93]
ORC	Turbine	$Z_{turbine} = 10^{2.62+1.43log(\dot{W}_t)-0.17\ (log(\dot{W}_t))^2}$	[43]
	Generator	$Z_{gen} = 60 \bullet \dot{W}_{net,ORC}^{0.95}$	[43]
	HX (evaporator/ condenser)	$Z_{HX} = 130 \bullet \left(\frac{A_{HX}}{0.093}\right)^{0.78}$	[94]
	Pump	$Z_{pump} = 3540 \bullet \dot{W}_p^{0.71}$	[43]
HDH	Humidifier	$Z_H = 317.46 \bullet V_H$	[95]
	Dehumidifier	$Z_D = 2143 \bullet A_D^{0.514}$	[96]
PEM		$Z_{PEM} = 1000 \bullet \dot{W}_{PEM}$	[43]

Note: $\dot{W}$ and $\dot{Q}$ in kW, A in m^2, and V in m^3.

$$PBP = \frac{CAPEX_{total}}{Revenue_{annual} - OPEX_{total}} \quad (112)$$

To numerically solve the economic model, specific operational limits, market prices, and financial assumptions must be defined. These parameters are comprehensively summarized in Table 10.

3.6.2. Environmental-economic benefit

The CO_2 mitigation benefit is calculated based on the displacement of grid-based electrolysis. Given the Egyptian grid emission factor (EF_{grid}= 0.4727 $kgCO_2/kWh$ [77]), the annual mitigated carbon mass (M^{mit}_{CO2}) is:

$$M^{mit}_{CO2}\ (kg/yr) = \dot{E}_{total} \cdot t_{op} \cdot EF_{grid} \quad (113)$$

where $\dot{E}_{total}$ is the total equivalent power recovered by the system.

Assuming a carbon credit price (P_{CO2}) of 40 USD/t CO_2 [105,106], the corresponding Carbon Credit Gain (CCG) is determined by [107]:

$$CCG\ (USD/yr) = \left(\frac{M^{mit}_{CO2}}{1000}\right) \bullet P_{CO2} \quad (114)$$

3.7. Simulation strategy and solution procedure

The comprehensive mathematical model described in the preceding sections has been fully implemented within the MATLAB computational environment. The simulation employs a sequential cascading strategy, replicating the thermodynamic degradation of the waste steam stream as it progressively depletes its latent heat content through partial condensation across the cascaded subsystems. Due to the coupled and non-linear nature of the governing equations—particularly within the TEG discretization and the PEM electrochemical model—a robust iterative solution algorithm is employed, the logic of which is visualized in the flowchart in Fig. 3.

The computational procedure initiates by defining the global boundary conditions, including the steam mass flow rate, inlet temperature range, and seawater intake conditions, alongside the fixed geometric and efficiency specifications for all subsystems. The solution sequence begins with the ORC subsystem, where the solver calculates the thermodynamic properties at the inlet (State 5) and resolves the Rankine cycle equations to determine the net power output and the intermediate state of the steam exiting the evaporator (State 6).

Subsequently, the simulation progresses to the TEG subsystem, where a discretized solver is applied to handle the non-linear temperature profiles. The duct is divided into 833 sequential control volumes; for each step, the system of coupled thermo-electrical equations is solved iteratively to determine the TEG surface temperatures and current. The steam enthalpy, quality, and cooling water temperature are updated dynamically for each subsequent module until the total TEG power, and the final steam condition (State 7) are computed.

Following the power generation stages, the solver internally transitions to the HDH desalination unit. The algorithm calculates the required thermal load needed to raise the seawater temperature to the specified Top Brine Temperature. By applying mass and energy balances across the humidifier and dehumidifier, the freshwater production rate is quantified, and the final state of the steam condensate (State 8) is defined.

Finally, the PEM electrolyzer model acts as the convergence point for the system's outputs. The total generated electrical power and the available freshwater are input into an electrochemical solver. An iterative loop estimates the initial cell voltage, calculates the resulting current density and overpotentials, and refines the voltage guess until convergence is achieved. Upon solving, the model outputs the final hydrogen production rate and evaluates the overall system efficiency.

Table 10
Economic parameters.

Parameter		Value	Unit	Ref.
Annual operating hours	t_{op}	8000	h/yr	[103]
Discount rate	r	10	%	
Project lifetime	N	20	yr	
O&M cost factor	$f_{O\&M}$	4	% of $CAPEX_{total}$	[33,104]
Miscellaneous cost factor	f_{misc}	15	%	

4. Results and discussions

This section presents the simulation results of the proposed integrated system based on the mathematical models described in the previous section. The analysis is divided into three main parts. First, the accuracy of the developed models is verified by comparing the results with experimental data and literature. Second, the overall system performance is evaluated under the design operating conditions. Finally, a parametric study is conducted to analyze the effect of varying the waste heat source inlet parameters and different organic working fluids on thermodynamic performance.

4.1. Component-level validation summary

To ensure the reliability of the developed hybrid computational framework, the numerical models of all four subsystems were rigorously validated against experimental data and established theoretical models from the literature. Table 11 and Fig. 4 provides a consolidated summary of the validation metrics across all subsystems, followed by a detailed discussion of each validation case.

Prior to experimental validation, the numerical implementation itself was independently verified. All nonlinear algebraic subsystems (ORC state-point solver, TEG thermal-electrical coupling, HDH humidifier/dehumidifier energy-mass balance, and PEM polarization solver) were solved using MATLAB's built-in iterative solvers with a convergence tolerance of 10^{-6} on all residuals, and solution independence from the initial guess was confirmed by perturbing initial conditions by ±20% and verifying convergence to identical state points in all cases. Energy and mass balance closure across each subsystem boundary was confirmed to within 0.01% at every simulated operating condition, and a run-to-run reproducibility check confirmed that the deterministic solvers produced bit-identical outputs across repeated executions. This verification step confirms that the reported results reflect a numerically converged and internally consistent solution, distinct from the subsequent experimental validation reported below.

It is acknowledged that direct experimental validation of the fully integrated four-stage system was not feasible within the scope of this work, as no published dataset exists for an identical ORC–TEG–HDH–PEM cascade configuration. However, the adopted modular validation approach — independently validating each subsystem against dedicated experimental benchmarks—ensures the robustness and physical accuracy of the overall integrated computational framework.

4.2. ORC, PEM, TEG, and HDH validation cases

(a) ORC subsystem

The thermodynamic model of the ORC subsystem is validated against the baseline reference data published by Zhang et al. [108]. The validation framework utilizes R245fa as the working fluid under standard cycle constraints: a condensation temperature (75 °C), an evaporation pressure (P_{evap}= 2.4 MPa), an isentropic pump efficiency (η_p =0.8), and an isentropic turbine efficiency (η_t =0.75). The comparative evaluation across all four thermodynamic state points is compiled in Table 12. The numerical results exhibit exceptional agreement, with a maximum relative error of 0.18% for fluid enthalpy and 0.03% for localized operating pressures, confirming the thermodynamic consistency of the cycle model.

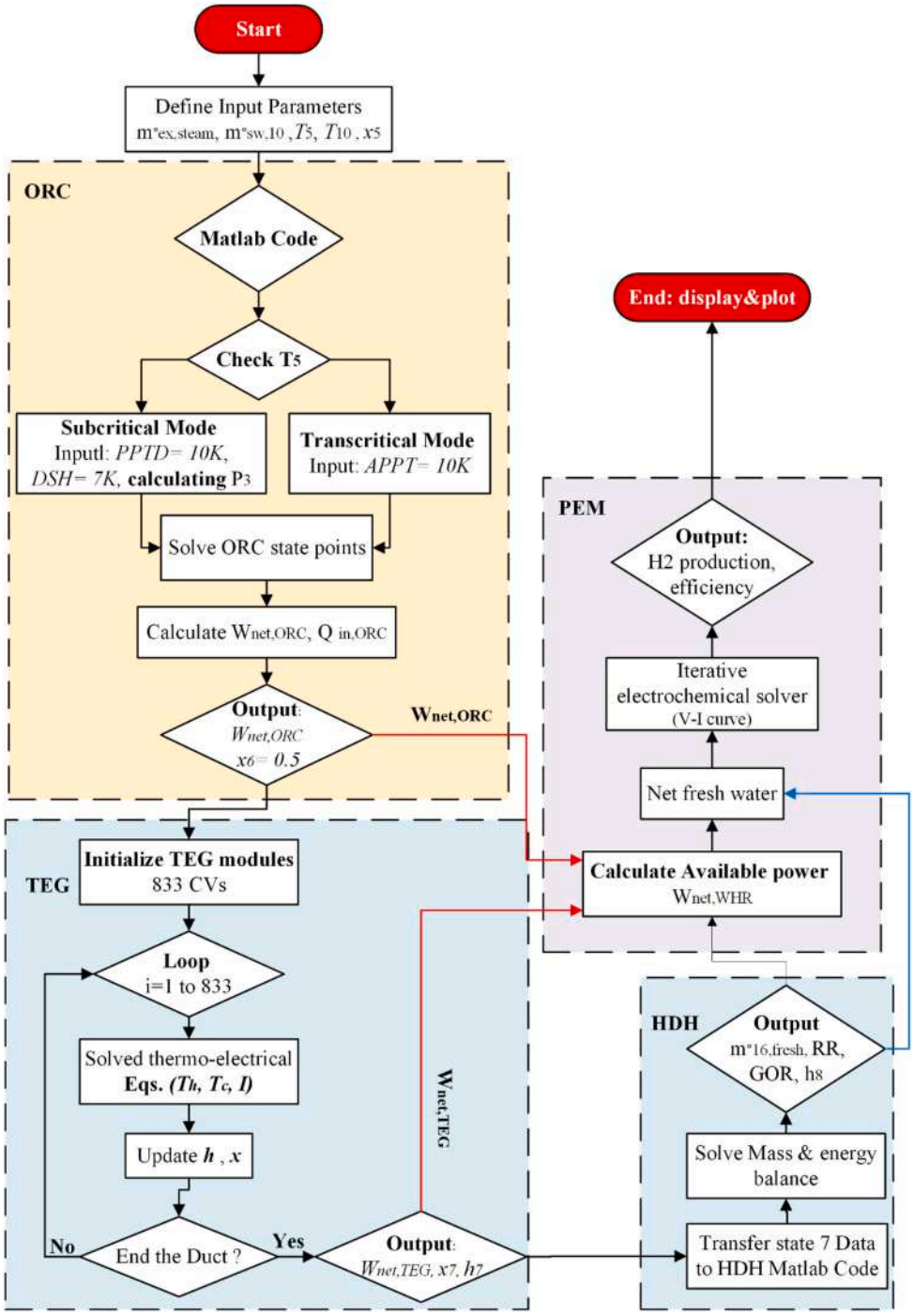

Fig. 3. Solution procedure flow chart.

Table 11
Summary of subsystem validation results.

Subsystem	Validated Against	Validation Metric	Error
ORC	State-point data, Zhang et al. [108]	Max. relative error	0.18%
PEM Electrolyzer	Polarization curve, Shoaib & Targhi [109]	MAPE	1.27%
TEG Module	I-V characteristics, TGM199–1.4-2.0 [4]	MAPE	1.36%
HDH Unit	GOR vs. MR, Sharqawy et al. [85]	MAPE	3.74%

(b) **PEM Electrolyzer**

The PEM electrochemical model is validated against experimental polarization data from Shoaib and Targhi [109] at T_{PEM} = 80 °C and atmospheric pressure. A constant electrical contact resistance was incorporated to account for interfacial losses, and the membrane water content was calibrated for a fully hydrated Nafion membrane. Fig. 4a compares the predicted polarization curve against experimental measurements across the full operating range (up to 5000 A/m^2), yielding a MAPE of 1.27%. This minimal deviation confirms that the combined Nernst–Butler-Volmer–ohmic formulation accurately captures the cell electrokinetic and ohmic losses across the full range of operating current densities.

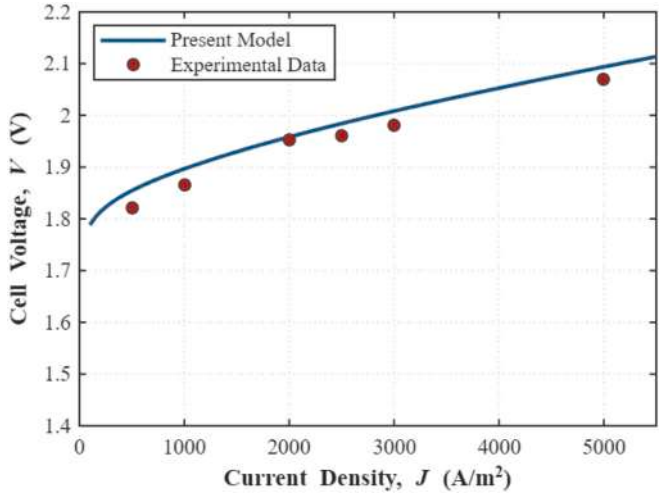

(a) PEM Electrolyzer

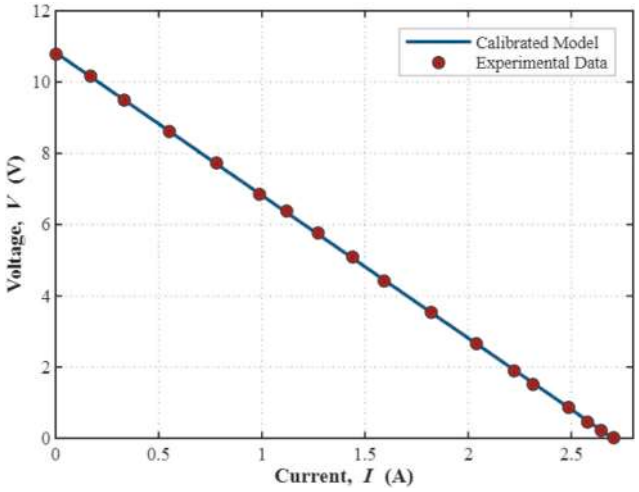

(b) TEG Module

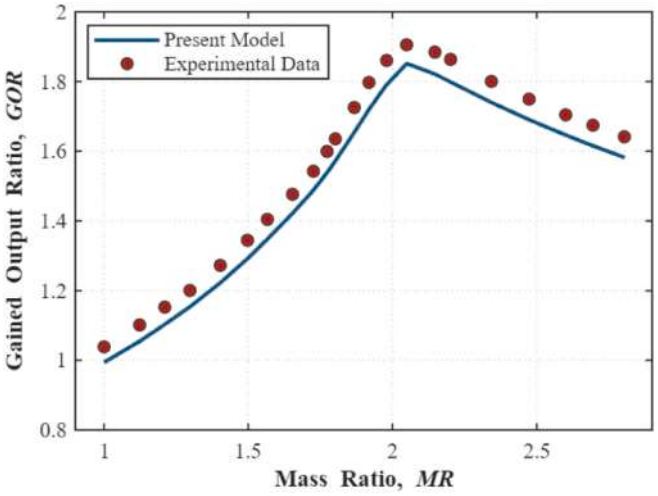

(c) HDH unit

Fig. 4. Validation of numerical sub-models against experimental data: (a) PEM electrolyzer polarization curve [110] (b) TEG I-V curve [4] (c) GOR variation with MR for HDH desalination [85].

Table 12
Comparison between the present ORC model results and reference data [108] for R245fa.

State	Pressure [MPa]			Enthalpy [kJ/kg]		
	Present	Zhang et al. [108]	Error	Present	Zhang et al. [108]	Error
1, *ORC*	0.695	0.695	0.03%	302.36	301.87	0.161%
2, *ORC*	2.4	2.4	0%	304.15	303.65	0.165%
3, *ORC*	2.4	2.4	0%	488.84	487.97	0.177%
4, *ORC*	0.695	0.695	0.03%	472.67	471.82	0.18%

(c) **TEG subsystem**

The thermoelectric conversion TEG model is validated against experimental data reported by [4] for a commercial TEG module (TGM199–1.4–2.0). Although the reference study investigates the module under fixed boundary temperature conditions ($T_h = 200^{\circ}C, T_c = 30^{\circ}C$), it serves as a robust benchmark to verify the accuracy of the Seebeck, Peltier, and Joule heating equations adopted in this study. Fig. 4b compares the current-voltage (I-V) characteristics obtained from the present model with experimental data. To rigorously quantify the accuracy of the prediction, the MAPE calculated. The results exhibit an exceptional agreement, yielding a MAPE of 1.36%. This highly minimal deviation firmly confirms the validity and reliability of the thermoelectric constitutive equations employed in the integrated simulation.

(d) **HDH subsystem**

Finally, The mathematical formulation characterizing the HDH thermal desalination block is validated against the experimental performance data reported by Sharqawy et al. [85] for a CAOW cycle. Humidification cycle. The validation baseline was established under documented reference conditions: top and bottom seawater inlet temperatures of 60 °C and 30°C, respectively, a dehumidifier outlet air relative humidity of 0.90, and a constant component effectiveness (ε) of

0.85 for both the humidifier and dehumidifier columns. Fig. 4c presents the comparison between the simulated and experimental GOR across a range of mass flow ratios. The numerical model achieves a highly acceptable fit with a MAPE of 3.74%. This minor deviation stems from the constant-effectiveness simplification, which cannot capture the effectiveness drift that real humidifier/dehumidifier packing exhibits under varying inlet conditions. This structural limitation, rather than the relative-humidity boundary condition, is the dominant source of residual deviation, and is consistent with comparable constant-effectiveness HDH validation studies reported in the literature [85].

4.3. Baseline system performance

With the computational framework rigorously validated, the study proceeds to evaluate the performance of the fully integrated polygeneration system. The following section presents the detailed thermodynamic analysis under the design operating conditions, serving as a baseline for the subsequent parametric investigations. Table 13 summarizes the input parameters and boundary conditions adopted for this baseline simulation. The waste heat source is assumed to be exhausted steam at 130 °C.

Under these specified conditions, the steady-state simulation results for the integrated system are presented in Table 14. The system effectively recovers the waste heat through the cascaded stages.

Table 14 provides a summary of the system's overall performance based on the proposed cascade strategy. In total, the system recovers 8.29 MW of thermal energy from the waste steam. When evaluating this performance, it is important to distinguish between the two defined metrics. The Overall System Efficiency (η_{sys}) appears relatively low at 7.21%, as it strictly accounts for the produced hydrogen, the highest form of energy in the system. However, this value does not tell the whole story. The EUF gives a more complete picture, reaching 34.33%. This higher figure reflects the system's ability to capture the significant value of the freshwater produced (latent heat), proving that the system effectively utilizes the resource even if the conversion to chemical energy (Hydrogen) is thermodynamically limited.

The energy distribution, shown in Fig. 5, follows the quality of the available heat. The majority of the recovered energy (71.87%) is consumed by the power generation stage (ORC & TEG) to maximize electricity output (696.55 kW) for the electrolyzer.

As the steam quality drops to 0.45, the HDH unit takes over, utilizing 25.94% of the total energy to secure a sustainable water supply with a GOR of 1.31. The cycle is completed by scavenging the last remaining fraction of low-grade heat (2.19%) to preheat the PEM feedwater to 80 °C. Notably, the system proves to be entirely self-sufficient in water. The PEM electrolyzer consumes only 3.7% of the generated freshwater,

Table 13
Design operating conditions and input parameters for the base case.

Subsystem	Parameter	Symbol	Value	Unit
Heat Source	Steam Inlet Temperature	T_5	130	$^\circ C$
	Steam Mass Flow Rate	$\dot{m}_5$	5	kg/s
	Steam Inlet Quality	x_5	1	–
ORC Cycle	Organic Fluid		R245fa	
	Degrees of Superheat	ΔT_{DSH}	5	K
	Pinch point temperature	ΔT_{PPTD}	10	K
	Condensing Temperature	T_{cond}	40	$^\circ C$
TEG Unit	Inlet Steam Quality	x_6	0.5	–
	Cooling Water mass flow rate	$\dot{m}_{cf,i}$	25	kg/s
	Cooling Water Temperature	$T_{cf,i}$	25	$^\circ C$
HDH Unit	Seawater Inlet Temperature	T_{10}	25	$^\circ C$
	Seawater Mass Flow	$\dot{m}_{10,sw}$	25	kg/s
	Air Relative Humidity	$\phi_{14,15}$	100	%
	Top Brine Temperature	T_{12}	70	$^\circ C$
	Mass Ratio	MR	2	–
	Component Effectiveness	ε	85	%
PEM Unit	Water Inlet Temperature	T_{17}	80	$^\circ C$

Table 14
Thermodynamic performance results of the integrated system at the design point.

Subsystem	Performance Indicator	Symbol	Value	Unit
Power Generation	ORC net power output	$\dot{W}_{net,ORC}$	675.06	kW
	TEG net power output	$\dot{W}_{net,TEG}$	21.49	kW
	Total net power supplied	$\dot{W}_{net,WHR}$	696.55	kW
	Steam quality leaving the TEG	x_7	0.452	–
Freshwater Production	Total freshwater rate	$\dot{m}_{16,fresh}$	3613	L/h
	Gained Output Ratio	GOR	1.312	–
	Steam quality leaving HDH	x_8	0.254	–
H_2 Production	Hydrogen production rate	$\dot{m}_{H2}$	15.17	kg/h
	PEM water consumption	$\dot{m}_{H2O,cons}$	135.6	L/h
	Excess freshwater	$\dot{m}_{H2O,excess}$	3477.40	L/h
	PEM system efficiency	η_{PEM}	64.31	%
	Steam quality leaving PEM	x_9	0.2376	
Overall System	Energy Utilization Factor	EUF	34.33	%
	Overall System Efficiency	η_{sys}	7.21	%
	Total thermal energy recovered	$\dot{Q}_{th,total}$	8286.14	kW

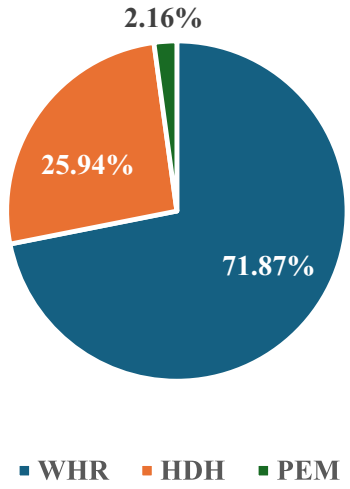

Fig. 5. Thermal energy recovery distribution among the integrated subsystems (WHR, HDH, and PEM heating).

leaving a significant net surplus of 3477 L/h available for export. Additionally, the PEM operates at an efficiency of 64.31%, which aligns well with standard commercial performance.

To fully justify the thermodynamic modeling of the TEG stage under the baseline conditions, the two-phase frictional pressure-drop analysis formulated in Eqs. (15)–(21) was numerically evaluated for the 833-module serpentine duct geometry at the design-point temperature of 130 °C. Each parallel duct features a rectangular cross-section area of A_{duct}, D_h = 0.0632 m and carries a per-duct steam mass flow rate $\dot{m}_{ex,steam,duct}$ of 0.417 kg/s. With an axial length of 0.04 m per module, consistent with the module footprint, the total continuous duct length (L) is 33.3 m. For the independent cross-check, the homogeneous mixture flow model was evaluated at the average steam quality across the duct ($\bar{x}$ = 0.476), which directly represents the physical transition from the inlet quality (x_6= 0.5) to the outlet quality (x_7= 0.452) obtained from the baseline simulation. Table 15 summarizes the resulting two-phase frictional pressure drop ($\Delta P_{two-phase}$) and the corresponding saturation-temperature shift (ΔT_{sat}) obtained from both the separated-flow framework and the homogeneous mixture model.

As indicated by the results, the two independent methods bound the expected saturation-temperature perturbation between 0.68 K and 3.14 K across the full duct length. Given that the heat source temperature is varied parametrically over a wide 110 K span (90–200 °C) in the subsequent sections of this study, this maximum estimated shift represents

Table 15
Two-phase frictional pressure drop across the 833-module TEG duct and the corresponding saturation-temperature shift, evaluated at the design-point source temperature of 130 °C.

Method	$\Delta P_{two-phase}$ [bar]	% of P_{sat}	ΔT_{sat} [K]
Separated-flow (Lockhart–Martinelli/ Chisholm)	0.254	9.38	3.14
Homogeneous mixture model	0.067	2.49	0.83

less than 3% of the entire investigated temperature range. This successfully confirms that the constant-saturation-temperature simplification adopted in the TEG thermal model introduces only a minor, second-order perturbation, validating the accuracy of the baseline performance trends without introducing unnecessary computational complexity.

4.4. Effect of heat source temperature, steam quality, and working fluid

To evaluate the system's performance under off-design conditions and identify the optimal operating strategy, this section examines the thermodynamic response to fluctuating heat source temperatures (90–200 °Cfor three candidate organic working fluids — R245fa, n-Pentane, and Cyclopentane — under two steam inlet qualities (0.8 and 1.0). All downstream operating parameters are held at their design values listed in Table 6.

4.4.1. Waste heat recovery (ORC + TEG) power and efficiency

Fig. 6 summarizes the WHR power generation profile over the heat-source temperature range investigated, presenting the individual subsystem power outputs (Fig. 6a) and the total integrated power generation (Fig. 6b).

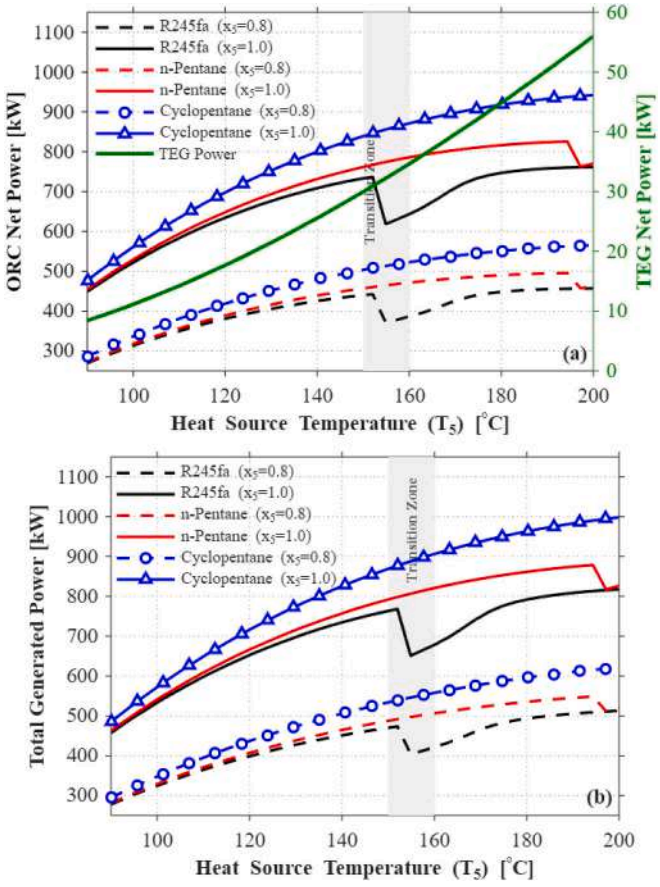

Fig. 6. Impact of varying heat source temperature on WHR subsystem performance: (a) net power output of each subsystem, (b) and total integrated WHR power output.

As shown in Fig. 6a, the ORC power output increases with source temperature for all working fluids. However, the shape of the performance curve is governed primarily by the proximity of each fluid to its critical temperature, whereas steam inlet quality mainly affects the magnitude of the generated power. At the lower bound of the investigated range (T_5= 90 °C), the three fluids exhibit similar performance, with Cyclopentane exceeding R245fa by only 6.2%. In contrast, increasing the steam quality from x_5 = 0.8 to x_5= 1.0 substantially increases power generation for all fluids due to the larger thermal energy available from saturated steam.

R245fa ($T_{critical}$ = 154.01 °C) exhibits a continuous increase in power output until the source temperature approaches its critical point. Beyond this region, the cycle transitions from subcritical to transcritical operation, producing a noticeable deterioration in performance. Table 16 summarizes the key thermodynamic state points across this transition.

The transition imposes a compound penalty on both sides of the cycle. On the compression side, the high-side pressure rises from 28.37 to 38.21 bar (+34.7%), increasing pump specific work from 2.49 to 3.43 kJ/kg (+37.9%). On the expansion side, turbine specific work falls from 38.31 to 25.44 kJ/kg (−33.6%), since supercritical heating provides a smaller enthalpy drop than subcritical phase-change evaporation. Together these effects reduce net specific work from 33.9 to 20.74 kJ/kg (−38.8%), producing a 16.07% power drop — from 442.26 kW ($\boldsymbol{x_5}$=0.8) / 737.10 kW ($\boldsymbol{x_5}$=1.0) at 152.1 °C, to 371.18 kW / 618.64 kW at 154.9 °C. That the drop is identical in percentage terms at both steam qualities indicates the instability originates in R245fa's thermophysical properties near the critical point, rather than in the fixed discharge-quality control strategy ($\boldsymbol{x_6}$= 0.5), which is unchanged across all temperatures.

n-Pentane ($T_{critical}$ ≈ 196.55 °C) exhibits a similar thermodynamic trend, but the transition occurs at a substantially higher temperature. As a result, the fluid maintains stable subcritical operation over a wider temperature range and outperforms R245fa throughout most of the intermediate region between 160 °C and 190 °C. However, as the source temperature approaches its critical point, n-Pentane experiences the same transition-induced degradation, with power output decreasing by 7.6% near 197.2 °C before recovering slightly at 200 °C. Cyclopentane, by contrast, maintains the highest net power output of the three fluids across the entire evaluated range (90–200 °C); no crossover between the Cyclopentane and n-Pentane power curves is observed, as Cyclopentane's combination of fully subcritical operation and superior thermophysical properties preserves its lead at every source temperature investigated. Consequently, the fluid avoids the compressibility effects associated with transcritical operation, resulting in a smooth and continuous increase in power output reaching 565.48 kW at x_5 = 0.8 and 942.47 kW at x_5 = 1.0 with no observable degradation.

In parallel with the ORC, the TEG subsystem provides crucial baseload stability. As shown in Fig. 6a, TEG power output climbs steadily with temperature—rising from 8.41 kW at 90 °C to a peak of 56.05 kW at 200 °C. Crucially, the power curves for different steam qualities

Table 16
Key ORC thermodynamic state points for R245fa across the subcritical-to-transcritical transition.

Parameter	150 °C (Subcritical)	156 °C (Near Critical)	162 °C (Transcritical)
Operating Mode	Subcritical	Transcritical	Transcritical
High-side Pressure [bar]	28.37	38.2	40.31
Turbine Inlet Temperature [°C]	145	150.8	156.2
Turbine Specific Work [kJ/kg]	38.31	25.44	28.77
Pump Specific Work [kJ/kg]	2.49	3.43	3.63
Net Specific Work [kJ/kg]	33.9	20.74	23.71
$\dot{W}_{net,WHR}$ [kW], x_5= 0.8	439.95	374.36	392.84
$\dot{W}_{net,WHR}$ [kW], x_5= 1	733.25	623.93	654.73

perfectly overlap. This stability validates the system's control strategy: by regulating the ORC to discharge steam at a fixed thermodynamic state ($x_6 = 0.5$), the TEG always receives a consistent heat flux regardless of upstream source enthalpy fluctuations.

Fig. 6b reflects the total integrated system output. Because the ORC dominates generation, the total power profile mirrors the ORC's behavior, amplified by the steam quality multiplier. For Cyclopentane at 200 °C, shifting from moderate (x_5= 0.8) to saturated steam conditions ($x_5 = 1.0$) drives the total aggregate power from 621.5 kW to a remarkable peak of 998.48 kW.

Fig. 7 illustrates the thermal efficiency evolution of the ORC and TEG subsystems across the investigated temperature range.

A critical observation from the ORC efficiency profiles is the perfect superposition of the curves for different steam inlet qualities ($x_5 = 0.8$ versus x_5= 1.0) for all three working fluids. This congruency indicates that ORC thermal efficiency is thermodynamically decoupled from the steam dryness fraction. While a higher steam quality increases the total heat input, the system's control logic triggers a proportional increase in the organic fluid's mass flow rate to absorb the extra load. Consequently, the net power output scales linearly with the heat input, canceling out the scaling factor and rendering efficiency strictly dependent on the source temperature and fluid properties.

Driven by these fluid properties, Cyclopentane demonstrates the highest thermodynamic performance, climbing steadily from 8.36% at 90 °C to a maximum of 19.43% at 200 °C. Its superiority stems directly from avoiding the severe high-pressure liquid pumping penalties that compromise the efficiencies of R245fa and n-Pentane near their critical points. Conversely, the TEG efficiency is driven purely by the magnitude of the temperature gradient across the modules. As the waste heat temperature rises to 200 °C, the intensifying Seebeck effect raises the TEG efficiency linearly to 6.38%. Like its power output, the TEG efficiency remains entirely immune to variations in upstream steam quality or working fluid selection, further confirming the resilience of the cascading architecture.

4.4.2. TEG duct pressure drop estimation

4.4.2.1. Control-parameter sensitivity of ORC performance. To assess the robustness of the performance hierarchy established above, Table 17 presents a one-at-a-time sensitivity analysis of the R245fa ORC net power output at two representative source temperatures—150 °C (subcritical) and 200 °C (transcritical)—under saturated steam conditions ($x_5 = 1.0$).

Turbine isentropic efficiency ($\eta_{turbine}$) is by far the most influential parameter: varying it between 0.75 and 0.95 changes net power by ±12.6% at 150 °C and ± 13.1% at 200 °C, consistent with its direct role in the turbine work term. The pinch-point, superheat, and approach temperature differences (PPTD, DSH, APTD) have a much smaller effect, with deviations no larger than −2.2%, and pump efficiency has a negligible influence (<1.5%) given the small pump work relative to turbine output in this range. None of these variations shift the onset of the R245fa transcritical instability near 154°C, confirming that the fluid ranking established in this study — and Cyclopentane's advantage in particular — is not an artifact of the chosen control parameters.

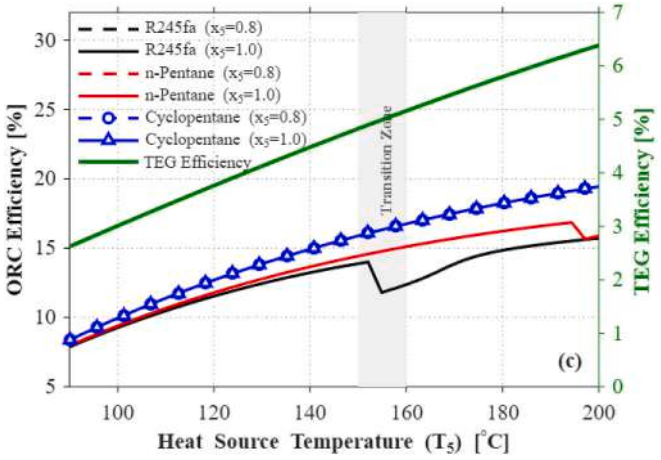

Fig. 7. Impact of varying heat source temperature on ORC and TEG efficiency

4.4.3. HDH desalination: Optimization and sensitivity

Before integrating the desalination unit with the upstream power generation stages, a parametric optimization was carried out to define its operating point, with the goal of maximizing thermodynamic efficiency (GOR) rather than freshwater volume alone.

Fig. 8 shows that this behavior depends on the thermal regime. At lower top brine temperatures (TBT = 50 °C and 60 °C), the GOR follows a parabolic trend with MR, peaking before declining due to airflow limitations; at higher TBT (70 °C and 80 °C), GOR instead increases monotonically over the studied MR range. At a fixed MR of 1, lower TBT consistently gives a higher GOR — 1.062 at 50 °C, falling to 0.841 at 80 °C — showing that lower brine temperatures use the available enthalpy more efficiently per unit of freshwater produced.

The global maximum is found at TBT = 50 °C and MR = 1.75, giving a GOR of 1.786, the highest in the study, with 2146 L/h of freshwater produced from 804.6 kW of thermal input. By comparison, TBT = 80 °C and MR = 2.5 gives a lower GOR of 1.277, despite a higher production rate of 4445 L/h, because the thermal demand nearly triples to 2299 kW.

TBT = 50 °C and MR = 1.75 was selected as the design point on efficiency grounds rather than production volume, for three reasons. First, it gives the highest GOR in the study, extracting the most freshwater per unit of low-grade heat in a cascade where every kilowatt of steam enthalpy is shared across four competing subsystems. Second, the PEM electrolyzer's freshwater demand — set by the upstream electrical power input — is a small fraction of the 2146 L/h produced at this point across all studied conditions (Section 4.4.4). Third, the alternative (TBT = 80 °C, MR = 2.5) would impose a thermal load of 2299 kW, nearly three times the 804.6 kW required at the selected point, leaving less residual steam enthalpy for the downstream PEM preheating stage and potentially compromising its operating temperature. The selected design point delivers freshwater at 37.83 °C, subsequently preheated to 80 °C in HX-2 using the HDH exhaust steam.

With the HDH thermal load fixed at 804.6 kW, freshwater production is fully decoupled from variations in the upstream heat source temperature across the full 90–200 °C range: the steam leaving the TEG subsystem always retains enough enthalpy surplus to meet the HDH demand, so the desalination stage acts as a stable anchor supplying a constant water stream to the PEM electrolyzer regardless of upstream fluctuations.

To address the practical variations in component performance, Table 18 presents a quantitative sensitivity analysis conducted by varying the humidifier and dehumidifier effectiveness ($\varepsilon_H, \varepsilon_D$) between 0.75 and 0.90 around the baseline design point $\varepsilon = 0.85$). As summarized in Table 17, under a severe component degradation scenario (ε = 0.75), the freshwater yield decreases by 20.69% (to 1702 L/h) and the GOR drops by 44.79% (to 0.986) due to the reduced latent heat recovery. Conversely, targeting an optimized design ($\varepsilon = 0.90$) enhances the freshwater yield by 12.53% (to 2415 L/h) and boosts the GOR by 53.19% (to 2.736).

Importantly, even under the worst-case degradation scenario (ε = 0.75), the freshwater output (1702 L/h) remains substantially higher than the maximum water consumption required by the PEM electrolyzer (197.68 L/h). This mathematically confirms that the assumption of fixed baseline effectiveness does not compromise the core conclusion regarding the system's absolute freshwater self-sufficiency.

To complement the parametric sensitivity analysis above with a formal uncertainty quantification, the propagated uncertainty in the

Table 17
Sensitivity of R245fa ORC net power to key control parameters ($x_5 = 1.0$).

Parameter [baseline]	Variation	T_5 = 150 °C (subcritical)		T_5 = 200 °C (transcritical)	
		$\dot{W}_{net,WHR}$ [kW]	$\Delta\dot{W}_{net,WHR}$ [%]	$\dot{W}_{net,WHR}$ [kW]	$\Delta\dot{W}_{net,WHR}$ [%]
ΔT_{PPTD} [10K]	5 K	744.056	+1.473	761.0167	0
	15 K	717.063	−2.21	761.0167	0
ΔT_{DSH} [5 K]	2.5	730.117	−0.43	761.0167	0
	7.5	735.593	+0.32	761.0167	0
ΔT_{APTD} [10 K]	5	733.252	0	769.104	+1.06
	15	733.252	0	748.309	−1.67
$\eta_{turbine}$ [0.85]	0.75	640.66	−12.63	661.078	−13.13
	0.95	825.844	+12.63	860.955	+13.13
η_{pump} [0.80]	0.70	726.625	−0.91	750.335	−1.40
	0.9	738.392	+0.701	769.286	+1.09

Note: Baseline $\dot{W}_{net,WHR}$ 733.25 kW at 150 °C | 761.02 kW at 200°C.

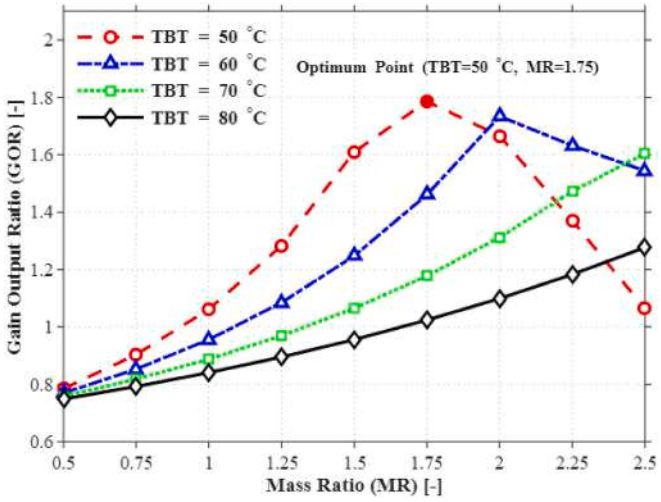

Fig. 8. Optimization of HDH performance: gain output ratio (GOR) as a function of mass flow ratio (MR) at varying top brine temperature (TBT).

Table 18
Sensitivity of the HDH desalination subsystem performance to variations in component effectiveness.

Effectiveness ε_H, ε_D	$\dot{m}_{16,fresh}$ [L/h]	$\Delta\dot{m}_{16,fresh}$ [%]	GOR	ΔGOR [%]
0.75 (Severe Degradation)	1702	−20.69%	0.986	−44.79
0.85 (Baseline Design)	2146	Reference	1.786	Reference
0.90 (Optimized Target)	2415	+12.53%	2.736	+53.19

reported baseline ORC net power output was estimated using the root-sum-square (RSS) method, combining representative instrument and correlation uncertainties for turbine efficiency (±2%), pump efficiency (±2%), pinch-point temperature difference (±0.5 K), and mass flow rate (±1%), consistent with typical industrial-grade sensor tolerances. The resulting propagated uncertainty in net ORC power output is approximately ±3.1% at the 200 °C design point (±31 kW on the reported 998.48 kW baseline). Applying the same procedure to the HDH freshwater yield, using effectiveness uncertainty of ±2% and seawater flowrate uncertainty of ±1%, gives a propagated uncertainty of approximately ±2.6% (±56 L/h) on the reported 2146 L/h design-point yield. These bounds are well within the margins established by the sensitivity analysis above and confirm that the reported fluid-selection ranking is robust to realistic combined measurement and modeling uncertainty.

4.4.4. PEM hydrogen production and water self-sufficiency

The second heat exchanger (HX-2) effectively utilizes the HDH exhaust's latent heat to raise the 2146 L/h freshwater feed to the PEM's 80 °C operating requirement. Consequently, the PEM operates under fully stable thermal conditions, meaning its performance is strictly governed by the upstream electrical power supply.

Fig. 9a illustrates the hydrogen production trends. At lower temperatures (90 °C), all fluids exhibit comparable yields (ranging from 6.58 to 6.96 kg/h at x_5=0.8). However, as the heat source temperature increases, the thermodynamic instability of R245fa and n-Pentane becomes highly visible; their transcritical dips severely bottleneck hydrogen output near 154 °C and 196 °C, respectively. Conversely, Cyclopentane ensures a smooth, monotonic production increase. Introducing saturated steam (x_5=1.0) substantially amplifies the yields across all fluids. At 200 °C, Cyclopentane achieves the absolute peak hydrogen production of 22.12 kg/h, outperforming R245fa (18.37 kg/h) and n-Pentane (19.65 kg/h) by roughly 24% and 12%, respectively, confirming that Cyclopentane's advantage expands at higher power levels.

Regarding operational sustainability, water consumption (Fig. 9b) scales linearly with hydrogen yield. Even at Cyclopentane's peak consumption of 197.68 L/h (x_5=1.0, 200 °C), the HDH unit secures a massive freshwater surplus of ~1948 L/h, thereby guaranteeing absolute feedstock self-sufficiency regardless of the selected fluid.

Meanwhile, Fig. 9c highlights a fundamental thermodynamic trade-off: as hydrogen production rises, the higher current density increases ohmic and activation losses within the stack, causing a slight decline in efficiency. For instance, Cyclopentane's efficiency drops from 65.57% at 90 °C to 62.77% at 200 °C. Thus, maximizing hydrogen yield inherently involves a minor, expected penalty in instantaneous electrolyzer efficiency.

4.4.5. Integrated system efficiency and energy utilization factor

The total thermal energy recovered ($\dot{Q}_{in,total}$) is the denominator for both the overall efficiency and EUF calculations. Because the ORC is controlled to a fixed discharge quality (x_6=0.5) and the desalination and PEM preheating loads are constant, $\dot{Q}_{in,total}$ depends only on the steam's inlet temperature and quality — and is therefore identical across all three working fluids.

$\dot{Q}_{in,total}$ itself shows opposite trends depending on inlet quality. At x_5=1.0, it falls from 7097.35 kW at 90 °C to 6797.02 kW at 200 °C, because the specific enthalpy of vaporization decreases as pressure rises toward the critical point, narrowing the saturation dome and reducing the latent heat available per unit mass. At x_5=0.8, Q_in instead rises slightly, from 4814.86 to 4857.29 kW, because TEG's heat extraction (proportional to ΔT) grows enough with source temperature to outweigh the modest reduction in latent content at this lower quality.

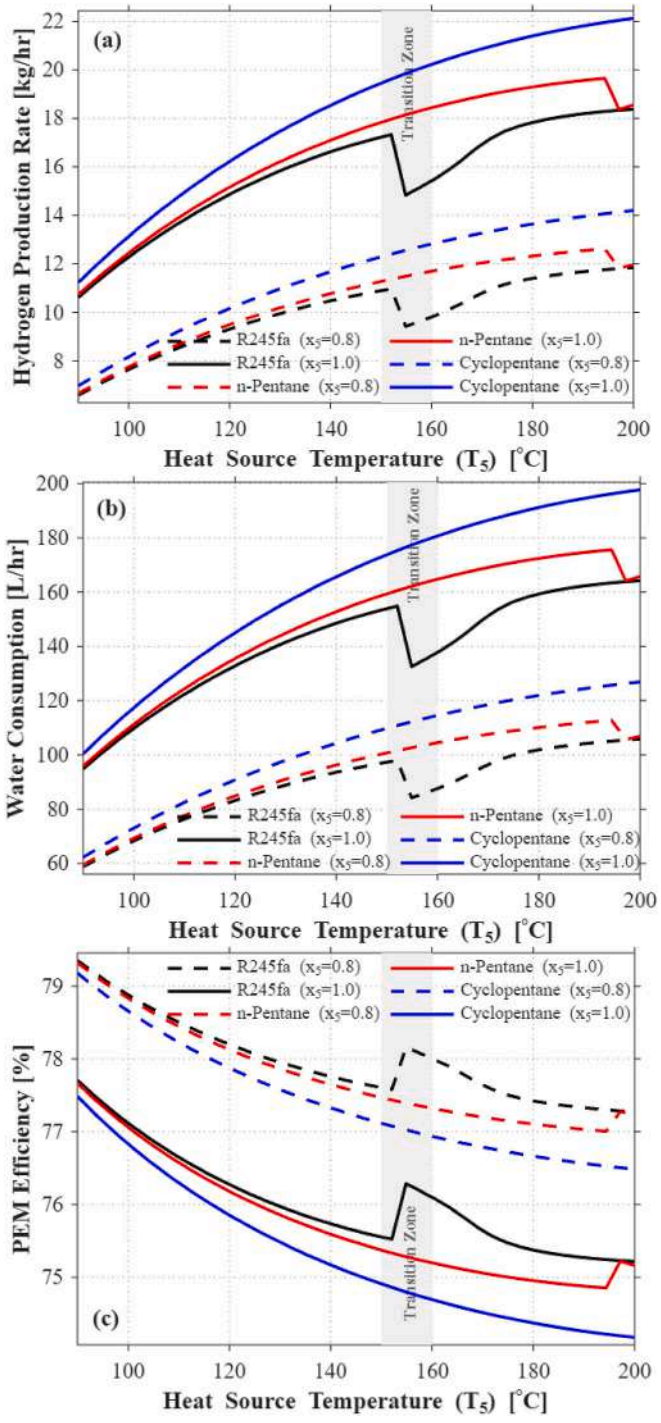

Fig. 9. Effect of heat source temperature, steam quality, and ORC working fluid on PEM electrolyzer performance: (a) hydrogen production rate, (b) water consumption, and (c) PEM efficiency.

Overall system efficiency (Fig. 10a) follows power generation trends, including the transcritical instability. At 90 °C and x_5=0.8, Cyclopentane leads marginally (5.697% vs. 5.449% for n-Pentane and 5.385% for R245fa). As temperature rises, R245fa peaks at 8.881% at 152.05 °C before dropping to 7.626% at 154.87 °C and recovering to 9.603% at 200 °C; n-Pentane peaks at 10.222% at 194.35 °C before dipping to 9.582% at 197.17 °C. Cyclopentane again rises smoothly, reaching 11.514% at 200 °C under x_5=0.8 and a global maximum of 12.82% under x_5=1.0.

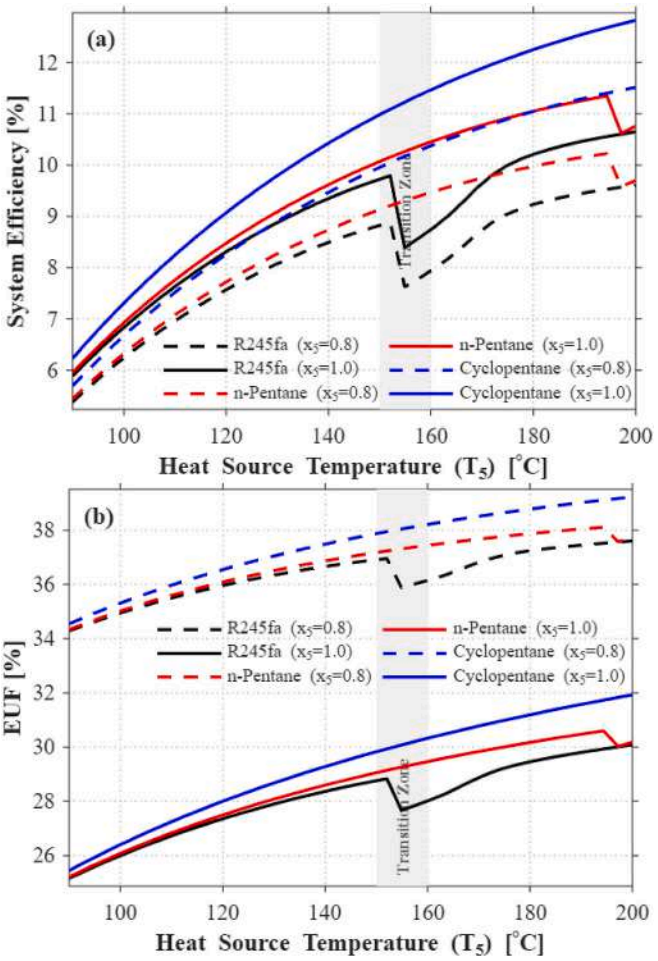

Fig. 10. Overall system performance across the 90–200 °C source temperature range: (a) overall system efficiency, and (b) energy utilization factor (EUF).

The EUF (Fig. 10b), which additionally credits the latent heat recovered as freshwater, shows the opposite ranking by steam quality: x_5=0.8 gives a higher EUF than x_5=1.0, despite delivering less power and hydrogen. At 200 °C, Cyclopentane reaches an EUF of 39.23% under x_5=0.8 versus 31.93% under x_5=1.0. This is a denominator effect: at x_5=1.0, Q_{in} is 6797 kW versus 4857 kW at x_5=0.8 (about 40% larger), while the HDH's 804.6 kW contribution to the numerator stays fixed, so it represents a smaller share of the total at higher quality even though absolute power and hydrogen output are higher. The two metrics therefore point to a genuine trade-off: high steam quality favors high-value outputs (electricity, hydrogen), while lower quality favors overall thermal resource utilization.

Across both metrics, Cyclopentane is the better-performing fluid, and — unlike R245fa and n-Pentane — achieves this without any transcritical instability over the full 90–200 °C range.

As discussed previously, Cyclopentane's sub-atmospheric operation imposes additional sealing and explosion-prevention requirements, which are weighed against its performance gains in the economic discussion below. Because Cyclopentane is an ASHRAE A3 (highly flammable) fluid, excluding oxygen from the sub-atmospheric zones is a safety requirement rather than an optional design choice, avoiding the risk of an internal explosive mixture. These requirements add capital cost and operational complexity relative to a positive-pressure fluid, but sub-atmospheric ORC operation is established industrial practice with mature, commercially available solutions. Given Cyclopentane's roughly 22% advantage in net power and hydrogen production over R245fa at 200 °C, and the complete elimination of transcritical instability across

the operating range, this added complexity is a reasonable trade for the gain in performance and operational robustness — making Cyclopentane the recommended working fluid for waste-heat-driven cascade hydrogen polygeneration systems in this temperature range.

Table 19 benchmarks the three fluids at 200 °C under both steam qualities. Under saturated steam, Cyclopentane delivers 998.48 kW of total net power — 22.1% and 20.7% above R245fa and n-Pentane respectively — and the highest hydrogen production at 22.12 kg/h (20.4% and 19.2% above R245fa and n-Pentane). At x_5=0.8, it also achieves the highest EUF (39.23%, versus 37.60% for R245fa and 37.70% for n-Pentane). The most consequential difference between the fluids, however, is operational stability: R245fa and n-Pentane both show transcritical power instabilities (16.07% and 7.6% respectively) within the studied range, while Cyclopentane's output increases monotonically throughout — a property that may matter more than peak efficiency for real systems exposed to variable waste steam conditions.

4.5. Second-law (exergy) assessment

4.5.1. Component-level exergy destruction

To pinpoint the exact sources of thermodynamic irreversibility within the cascade, an exergy destruction breakdown was performed. Fig. 11 illustrates the component-level exergy destruction at the baseline heat source temperature of 130 °C (x_5 = 1.0). At this specific operating point, the HDH unit and the ORC evaporator clearly dominate the irreversibility profile across all working fluids. The HDH unit destroys a constant 338.78 kW, driven primarily by the finite temperature differences within its seawater preheater. Meanwhile, the evaporator's exergy destruction is fluid-dependent, with Cyclopentane exhibiting the lowest destruction (256.68 kW) due to its superior thermal matching, and R245fa exhibiting the highest (329.61 kW) as it operates closer to its critical point.

However, expanding this analysis across the full sensible heat range (90–200 °C) reveals a dynamic shift in the system's thermodynamic bottlenecks, as summarized in Table 20. Because the HDH unit operates at a fixed design condition to satisfy a specific freshwater demand, its exergy destruction remains invariant. In contrast, the ORC evaporator's irreversibility scales dramatically with the heat source temperature, ranging from 182.9 kW at 90 °C to a peak of 618 kW at 200 °C. Consequently, while the HDH unit is the primary exergy destroyer at lower source temperatures, the evaporator overtakes it at elevated temperatures. Together, these two heat-exchange-dominated components represent the core targets for any future geometric or operational optimization. The remaining subsystems—namely the PEM electrolyzer, TEG, turbine, and condenser—contribute progressively less to the total exergy destruction, with the pump being the most thermodynamically reversible component across all scenarios.

Table 19
Comparative performance of the three ORC working fluids at T_5= *200 °C.*

Parameter	x_5	R245fa	n-Pentane	Cyclopentane
ORC Net Power (kW)	0.8	457.08	462.45	565.5
	1	761.81	770.78	942.47
Total Net Power (kW)	0.8	513.1	518.5	621.5
	1	817.82	826.8	
H_2 Production (kg/h)	0.8	11.84	11.96	14.2
	1	18.37	18.56	22.12
Freshwater Surplus (L/h)	0.8	2040.2	2039.12	2019.12
	1	1981.8	1980.1	1948.32
Overall Efficiency η_{sys} (%)	0.8	9.6	9.7	11.5
	1	10.65	10.76	12.82
EUF (%)	0.8	37.6	37.7	39.23
	1	30.1	30.2	31.93
Transcritical Instability	–	Yes (16.07%)	Yes (7.6%)	No
Peak Power Drop Temperature	–	~154°C	~196 °C	–

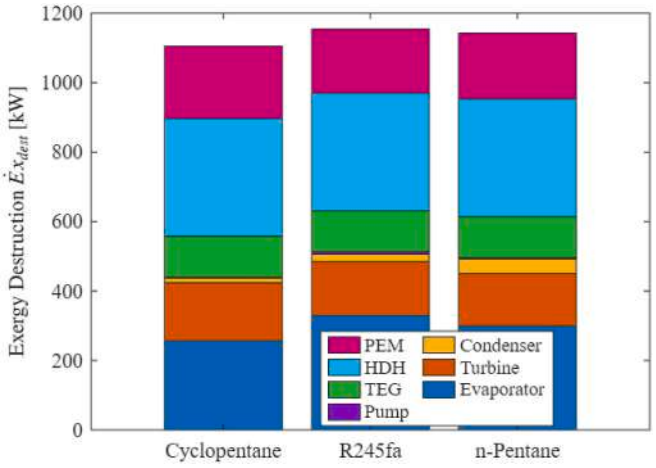

Fig. 11. Component-level exergy destruction at the design-point temperature (T_5= *130 °C, x_5 = 1.0*).

4.5.2. Exergetic efficiency and working-fluid comparison

Translating these irreversibilities into second-law efficiencies (ψ) provides a normalized measure of how effectively each subsystem utilizes its available work potential, Table 21 summarizes the subsystem and overall second-law efficiencies at basic case (T_5= 130 °C, x_5 = 1.0). The PEM electrolyzer emerges as the most exergetically efficient subsystem (ψ_{PEM} > 73%), reflecting the inherently low entropy generation associated with converting pure electrical exergy into chemical bonds (hydrogen). Conversely, the HDH unit, despite its acceptable first-law performance, exhibits a near-zero second-law efficiency (ψ_{HDH}= 0.19%). This stark contrast underscores a fundamental thermodynamic reality: while the HDH effectively recovers latent thermal energy, its final product (near-ambient liquid water) possesses negligible exergy relative to the high-grade heat consumed.

At the system level, Fig. 12 maps the overall exergetic efficiency (ψ_{sys}). The trends perfectly align with the component-level findings: Cyclopentane consistently achieves the highest overall second-law efficiency, peaking at 18.20% near 130 °C, outperforming both n-Pentane and R245fa. As the heat source temperature increases beyond this optimum, ψ_{sys} gradually declines for all fluids, directly mirroring the exponentially rising exergy destruction within the ORC evaporator (Table 19). Furthermore, reducing the waste steam quality to x_5= 0.8 noticeably depresses ψ_{sys} across the board, confirming that moisture content not only reduces total energy input but actively degrades the thermodynamic quality of the heat source.

4.6. Techno-economic and environmental performance

4.6.1. Levelized cost of hydrogen and profitability (NPV, PBP)

The economic viability of the proposed system was comprehensively assessed using the LCOH metric across a temperature sweep of 90–200 °C for three distinct working fluids (R245fa, n-Pentane, and Cyclopentane). As illustrated in Fig. 13, a consistent downward trend in LCOH is observed for all candidates as the heat source temperature increases, primarily driven by the exponential enhancement in net power output and subsequent hydrogen production yields which outweigh the associated incremental increase in CAPEX.

Among the evaluated fluids, Cyclopentane demonstrates a clear thermodynamic and financial supremacy across the entire thermal range. At the lowest boundary of 90 °C, Cyclopentane yields an LCOH of 2.215 USD/kg, compared to 2.272 USD/kg for n-Pentane and 2.305 USD/kg for R245fa.

As the source temperature escalates to 200C, Cyclopentane achieves the optimum (lowest) LCOH of 1.783 USD/kg, representing a substantial reduction that underscores its suitability for high-temperature WHR.

Table 20
Exergy destruction ranking across the studied temperature range (*90–200 °C, $x_5 = 1.0$*).

T_5 [°C]	Fluid	$\dot{E}x_{dest.evap}$ [kW]	$\dot{E}x_{dest.turb}$ [kW]	$\dot{E}x_{dest.cond}$ [kW]	$\dot{E}x_{dest.pump}$ [kW]	$\dot{E}x_{dest.TEG}$ [kW]	$\dot{E}x_{dest.PEM}$ [kW]
90	R245fa	206.87	102.57	9.722	2.61	50.66	112.29
110		261.65	133.25	15.88	4.53	81.68	153.44
130		329.61	155.14	21.073	6.99	117.91	184.43
150		408.5	170.83	22.22	10.20	158.66	205.94
170		503.58	185.63	2.849	16.77	203.43	210.25
200		575.97	176.17	63.01	16.04	277.43	230.65
90	n-Pentane	199.16	101.21	15.026	1.322	50.66	113.78
110		244.82	130.69	27.5	2.27	81.68	156.57
130		299.3	150.79	42.41	3.43	117.91	189.88
150		357.23	163.92	58.23	4.83	158.66	215.03
170		415.73	171.88	72.85	6.48	203.43	233.24
200		617.71	190.76	4.73	14.45	277.43	231.83
90	Cyclopentane	182.92	107.75	3.83	0.74	50.66	120.17
110		215.41	142.12	7.96	1.31	81.68	168.7
130		256.68	166.79	14.23	2.03	117.91	208.27
150		301.9	183.68	22.43	2.93	158.66	239.64
170		347.7	194.33	31.96	3.98	203.43	263.64
200		412.88	201.33	46.33	5.89	277.43	287.39

Table 21
Second-law (exergetic) efficiencies at $T_5 = 130$ °C, $x_5 = 1.0$.

Subsystem	ψ_{R245fa} [%]	$\psi_{n-Pentane}$ [%]	$\psi_{Cyclopentane}$
ORC	47.8	49.04	53.22
TEG	19.22	19.22	19.22
HDH	0.191	0.191	0.191
PEM	73.82	73.71	73.35
Overall System	16.52	16.91	18.2

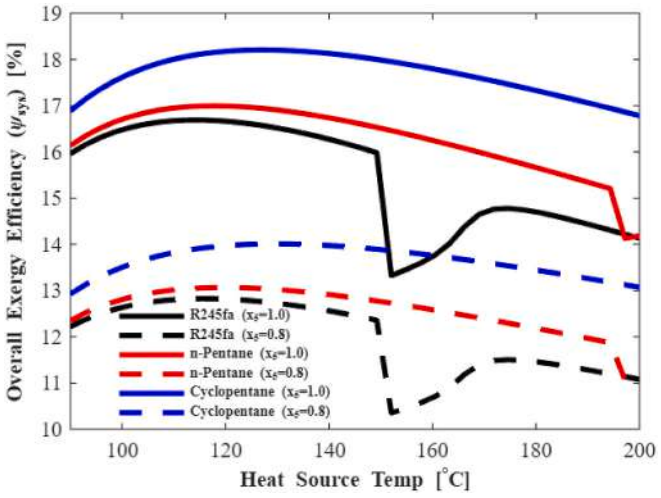

Fig. 12. Variation of the overall system second-law with respect to the heat source temperature (90–200 °C) for the investigated working fluids.

Conversely, R245fa exhibits an economic plateau beyond 150 °C due to its lower critical temperature, causing its LCOH to experience a slight penalty at 170 °C (1.975USD/kg) before settling at 1.945 USD/kg at 200 °C.

To project the long-term financial health of the plant over its 20-year operational lifespan, the NPV was simulated at a fixed 10% discount rate. Fig. 14 depicts the cumulative discounted cash flow curves, highlighting the profound divergence between the conservative conditions (90 °C) and optimized thermal conditions (200 °C).

All simulated configurations yielded positive NPV values by Year 20, verifying the baseline feasibility of the system. In alignment with the LCOH findings, Cyclopentane at 200 °C establishes the absolute highest fiscal yield, culminating in a dominant 20-year NPV of approximately

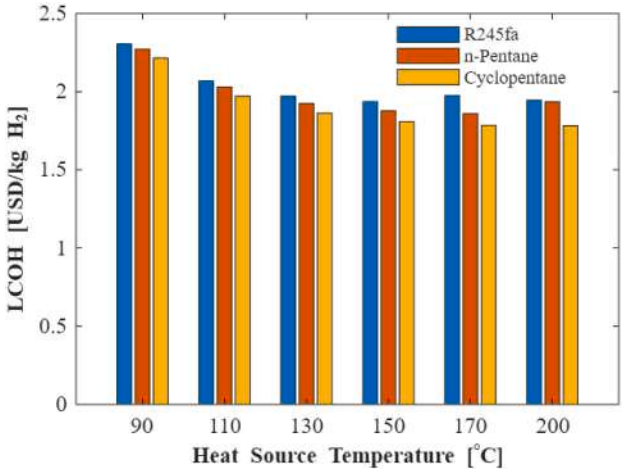

Fig. 13. The Levelized Cost of Hydrogen (LCOH) for different working fluids across the evaluated heat source temperature range at a standardized thermal source quality ($x_5 = 1.0$).

4967.5 kUSD. This massive return is heavily supported by its high net annual cash flow, driven by an annual hydrogen output of 181,380 kg. In contrast, even under the worst-performing scenario—namely R245fa at 90 °C—the system still generates a healthy lifecycle NPV of 1955.3 kUSD, which confirms that the integration of the TEG-ORC-PEM architecture acts as an economically resilient waste-to-fuel pathway regardless of minor fluid or thermal fluctuations.

Table 22 establishes the parametric link between capital investment and the actual velocity of capital return through the PBP. A critical trade-off is evident: higher source temperatures inherently command larger total CAPEX figures due to the required expansion of heat exchanger surface areas and sub-system scaling (e.g., Cyclopentane CAPEX rises from 1268.4 kUSD at 90 °C to 2053.9 kUSD at 200 °C).

However, the capital return rate accelerates markedly at elevated temperatures. The PBP for Cyclopentane drops steadily from 3.1709 years at 90 °C to an exceptionally rapid 2.4904 years at 200 °C. This behavior indicates that the revenue generated from high-capacity hydrogen sales far outpaces the heightened initial investment. For n-Pentane and R245fa, the shortest achieved payback periods are 2.6068 years (at 170 °C) and 2.7271 years (at 150 °C), respectively, signaling that both alternative fluids face premature performance diminishing returns at the upper boundary of the thermal scope.

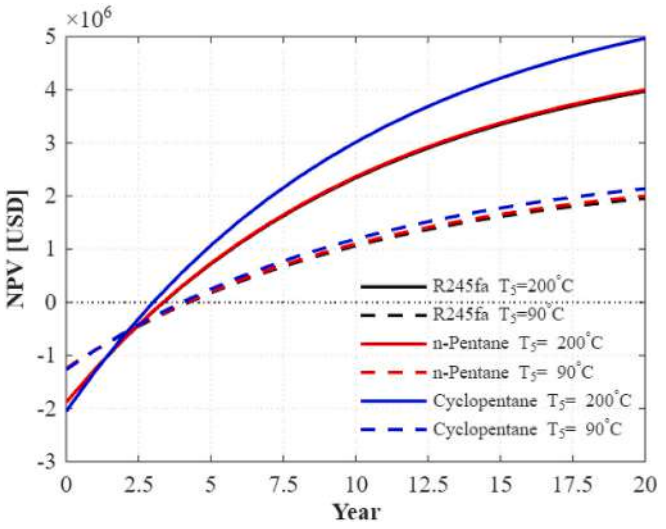

Fig. 14. Net Present Value (NPV) profiles over the 20-year project lifetime comparing conservative (90 °C) and (200 °C) waste heat grades for R245fa, n-Pentane, and Cyclopentane.

Table 22
Techno-economic performance metrics, capital investment summary (CAPEX), lifecycle NPV, and payback period (PBP) comparison for the selected working fluids at distinct waste heat grades.

Temperature [°C]	Fluid	CAPEX [kUSD]	LCOH [USD/ kg]	NPV [kUSD]	PBP [yr]
90	R245fa	1247.6	2.305	1955.3	3.316
	n-Pentane	1243.3	2.272	2000.9	3.263
	Cyclopentane	1268.4	2.215	2137.1	3.171
130	R245fa	1599.8	1.971	3296.2	2.782
	n-Pentane	1599.2	1.925	3425.6	2.709
	Cyclopentane	1665.9	1.862	3762.6	2.613
170	R245fa	1780.4	1.975	3654.6	2.789
	n-Pentane	1818.5	1.858	4120.6	2.607
	Cyclopentane	1923.1	1.785	4642.0	2.494
200	R245fa	1886.4	1.945	3971.9	2.741
	n-Pentane	1883.0	1.934	4002.8	2.724
	Cyclopentane	2053.9	1.783	4967.5	2.490

4.6.2. Carbon mitigation and credit valuation

The environmental merits of substituting conventional fossil-dependent power with the integrated system were quantified based on the displacement of the Egyptian electricity grid emission factor (0.4727kgCO2/kWh). As summarized in Table 23, the system delivers substantial carbon mitigation vectors that scale linearly with the total electrical power routed to the PEM electrolyzer stack.

Once again, Cyclopentane provides the most robust environmental mitigation profile. At a design temperature of 200 °C, the Cyclopentane-fueled configuration sustains an aggregate power output of 998.481 kW, translating directly into 3775.8 tons of avoided CO2 emissions annually. Under a standardized carbon taxation/credit evaluation of 40 USD/t, this level of decarbonization unlocks a supplemental CCG of 151,034.2 USD/yr. Even at the minimum waste heat grade of 90 °C, the system prevents the release of at least 1729.4-ton CO2 per year across all fluids. These indices definitively elevate the proposed system from a purely profitable thermodynamic utility to a powerful tool for industrial decarbonization.

4.7. Benchmarking against prior polygeneration literature

Conventional ORC–PEM hydrogen production systems driven by industrial waste heat, such as cement plant exhaust (360–780 °C) and refinery streams (~171 °C), typically report relatively low overall energy efficiencies in the range of approximately 8.62%–14.45% [43,111]. In comparison, the proposed TEG–ORC–HDH–PEM cascade achieves a significantly higher overall energy efficiency of 12.82%, despite operating under substantially lower-grade heat conditions (90–200 °C), as summarized in Table 24. This demonstrates the effectiveness of the proposed multi-stage thermal cascading strategy in maximizing useful exergy extraction from low-temperature resources.

From an economic perspective, the proposed system achieves a hydrogen production cost of 1.783 USD/kg, which is lower than most reported renewable- and waste-heat-based hydrogen systems, including biomass-driven ORC–PEM configurations (1.74 USD/kg [112]) and refinery-based ORC–PEM systems (2.36 USD/kg [111]), while remaining significantly more competitive than solar- and wind-based hydrogen

Table 23
Environmental decarbonization vectors, electrical power allocation, and simulated Carbon Credit Gains (CCG) for the integrated system.

Temperature [°C]	Fluid	$\dot{W}_{net,WHR}$ [kW]	M^{mit}_{CO2} [t/yr]	CCG [USD/yr]
90	R245fa	457.332	1729.4	69,177.8
	n-Pentane	462.631	1749.4	69,979.4
	Cyclopentane	485.255	1835.0	73,401.6
130	R245fa	695.791	2631.2	105,248.1
	n-Pentane	713.304	2697.4	107,897.2
	Cyclopentane	771.987	2919.3	116,773.8
170	R245fa	742.227	2806.8	112,272.2
	n-Pentane	841.829	3183.4	127,338.4
	Cyclopentane	934.667	3534.5	141,381.4
200	R245fa	817.817	3092.6	123,706.2
	n-Pentane	826.792	3126.6	125,063.8
	Cyclopentane	998.481	3775.8	151,034.2

Table 24
Comparative benchmarking of the proposed system's performance against recent polygeneration and waste-heat recovery literature.

Ref	System description	LCOH [USD/ kg_{H2}]	Main findings
[43]	Rankine cycle + PEM / SOEC electrolyzer	1.55–1.63	At 360 °C • H_2 production = 19.96 kg/h • η_{en} = 12.88%. At 780 °C • H_2 production = 22.4 kg/h • η_{en} = 14.45%.
[112]	Biomass waste heat + RC/ORC + PEM	1.74	H_2 production = 93.81 t/yr
[113]	PV/Wind + PEM	3.73–4.66	H_2 production = 1912 kg/yr η_{en} = 16.42%; η_{ex} = 12.76%; PBP = 7–13.85 years
[114]	Solar tower + Brayton + ORC + PEM + absorption chiller	7.01	15.8% enhancement in H_2 production accompanied by a 4.2% reduction in H_2 production cost.
[115]	PV, PVT, WT and hybrid renewable systems + PEM	2.84	$\eta_{en} \approx 35\%$ $\eta_{ex} \approx 17\%$ Electricity demand = 56.17–56.87 kWh/kg_{H2}
[111]	Low-grade refinery waste heat + ORC + PEM	2.36	H_2 production = 304.53 t/yr η_{en} = 8.62% η_{ex}= 33.43%
[116]	Geothermal + CSPVT + Wind + H_2 subsystem	28.86	H_2 production = 0.249 kg/h η_{en}= 48.61% η_{ex} = 88.31%
Present System	Condensing steam + ORC + TEG + HDH + PEM	1.783	H_2 production = 22.12 kg/h η_{en}= 12.82% η_{ex} = 18.2% EUF = 39.23% Electricity demand = 45.14 kWh/kg_{H2}

systems (2.84–7.01 USD/kg [113–115]). Only SOEC-based high-temperature cement waste heat systems report comparable or slightly lower cost values (~1.55–1.63 USD/kg [43]), but these operate at substantially higher temperature levels (up to 780 °C) and do not include integrated desalination or thermoelectric enhancement. In terms of system utilization performance, the proposed configuration achieves an EUF of 39.23%, reflecting the combined contribution of electricity, hydrogen, and freshwater outputs. While certain multi-source renewable systems report higher overall efficiencies (e.g., 48.61% for a CPVT–wind–geothermal hybrid system [116]), such configurations rely on multiple external renewable inputs rather than a single waste-heat-driven energy source. Therefore, direct comparison should consider the difference in energy input structure and system boundary definition. Overall, when considering low-grade waste heat-to-hydrogen-and-water polygeneration systems, the proposed architecture demonstrates a favorable balance between thermodynamic efficiency, hydrogen production cost, and system integration complexity, achieved through a unique four-stage cascade (ORC–TEG–HDH–PEM) that has not been previously reported in the literature.

4.8. Practical implementation: Scalability, control, and maintenance

Regarding system scalability, the proposed cascade architecture operates on a modular and inherently linear basis. Based on the peak thermodynamic performance achieved with Cyclopentane at the baseline 5 kg/s industrial waste steam flow, the system generates 998.48 kW of electrical power to yield 22.12 kg/h of hydrogen, consuming 197.68 L/h of ultra-pure water. Consequently, the system establishes fixed operational ratios: a specific energy consumption of approximately 45.14 kWh per kg of hydrogen, and a water consumption of 8.94 Liters per kg of hydrogen.

While the present framework establishes water self-sufficiency on a volumetric basis, the freshwater distillate produced by the HDH unit is not modeled at the ionic-conductivity specification typically required by commercial PEM membranes; a final polishing stage, such as mixed-bed deionization, would therefore be necessary in a practical deployment, with its associated energy and capital cost not included in the present balance. The PEM stack is evaluated only at steady-state design points across the investigated source-temperature range, and its transient load-following response under fluctuating industrial waste-steam availability is addressed in the System Limitations.

Adapting the system to larger industrial waste steam conditions (e.g., scaling up to 20 or 50 kg/s) will proportionally amplify the hydrogen yield and water demand. However, this imposes direct footprint constraints: the ORC will require larger turbomachinery, the HDH unit's packing volume must increase, and the TEG subsystem must utilize parallel modular assemblies to accommodate higher steam volumes while preventing severe aerodynamic pressure drops.

To reliably manage these scalability dynamics and variable industrial conditions, the integrated system necessitates a sequential cascade control strategy coordinated by a supervisory SCADA system. The primary control loop modulates the ORC mass flow rate in real-time—via a VFD on the pump—to maintain the fixed outlet steam quality ($x_6 = 0.5$), ensuring stable TEG inlet conditions. While the solid-state TEG subsystem requires no active control, the HDH unit operates at a fixed seawater flow rate with its Top Brine Temperature regulated via a motorized steam supply valve. Finally, the PEM electrolyzer's power input is passively determined by the synchronized DC upstream electrical output.

Beyond control logic, continuous industrial deployment introduces specific maintenance and operational constraints. The primary deployment prerequisite is the continuity of the waste heat source; facilities with highly intermittent batch processes are fundamentally incompatible with the stable baseload requirements of both the TEG array and the PEM electrolyzer. Furthermore, long-term operation necessitates proactive maintenance: the TEG modules are susceptible to heat sink fouling and thermal cycling fatigue, the HDH humidifier packing requires periodic replacement due to seawater scaling, and the PEM stack faces inherent membrane degradation over time. By incorporating standard industrial inspection for the ORC turbomachinery, these mechanical and chemical maintenance challenges can be systematically mitigated.

5. Conclusion

The study demonstrates that a four-stage, fully integrated system utilizing ORC, TEG, HDH, and PEM units can recover thermal energy from industrial exhaust steam to provide both electrical power and high-purity water needed for hydrogen production, all driven by a single waste steam stream. By systematically examining working fluids, the research addresses the critical operational instability observed with R245fa and n-Pentane under subcritical–transcritical regime crossings and establishes criteria for fluid selection in environments with variable temperatures. The MATLAB–CoolProp modeling approach accurately captures dynamic thermodynamic and electrochemical behaviors from 90 °C to 200 °C. The main findings are summarized as follows:

- At higher temperatures, R245fa and n-Pentane experience performance drops of 16% and 7.6%, respectively, due to critical-point effects. Conversely, Cyclopentane's fully subcritical operation maintains consistent power increases and achieves the highest output throughout the temperature range. At 200 °C, Cyclopentane's ORC power peaks at 998.48 kW, significantly outperforming the other fluids and highlighting the importance of avoiding transcritical instability.
- The TEG subsystem output rises linearly with temperature and remains unaffected by fluid type or steam quality, thanks to controlled inlet conditions, emphasizing robust system design.
- The HDH stage provides a stable freshwater output and maintains optimal efficiency at 50 °C, effectively supporting the electrolyzer with a considerable surplus of water across all tested ranges.
- Cyclopentane delivers the best performance, converting up to 998.48 kW into a maximum hydrogen yield of 22.12 kg/h. This results in roughly 12% higher hydrogen output than n-Pentane and 24% more than R245fa, confirming that Cyclopentane offers the greatest benefits at high power levels.
- Although PEM efficiency slightly decreases at higher temperatures, the increased hydrogen production and excess water supply—well within HDH capabilities—ensure the system's operational independence.
- The highest overall efficiency and energy utilization factors are achieved with Cyclopentane, reaching 12.82% efficiency at saturated conditions and a peak EUF of 39.23% at 200 °C, underscoring the importance of fluid choice and steam quality adjustments for maximizing thermal resource utilization.
- Exergy analysis identifies the HDH seawater preheater and the ORC evaporator as the dominant sources of irreversibility across the cascade, while the PEM electrolyzer operates closest to its thermodynamic limit (>73% efficiency). Cyclopentane consistently achieves the highest overall second-law efficiency (16.78–18.20%), confirming that its superiority extends beyond merely maximizing power output to encompass a genuinely more reversible and thermodynamically sustainable system operation.
- Cyclopentane emerges as the most economically lucrative and environmentally robust candidate, achieving a remarkably short payback period of 2.49 years and an absolute maximum 20-year NPV of 4967.5 kUSD at 200 °C. Furthermore, its superior power allocation capacity drives an annual grid-decarbonization vector of 3775.8 tons of avoided CO2 emissions, unlocking an additional CCG of 155,103.4 USD/yr and reinforcing the system's alignment with global industrial sustainability goals.

6. System limitations and future directions

First, the present study adopts a steady-state mathematical modeling framework by design, consistent with the objective of establishing baseline thermodynamic performance envelopes and fluid-selection criteria across the full 90–200 °C source-temperature range — a scope choice standard in early-stage polygeneration feasibility studies before transient controller design is undertaken. Within this steady-state framework, the closed-loop control *architecture* (the PID/VFD-actuated mass-flow modulation maintaining ORC outlet steam quality at $x_6 = 0.5$, and the motorized-valve-regulated HDH Top Brine Temperature) is explicitly modeled as the mechanism that enforces the fixed inter-stage boundary conditions reported in Table 1; however, the *dynamic response* of these control loops — including actuator response time, controller gain tuning, and closed-loop stability margins under time-varying thermal input — has not been simulated and is explicitly outside the scope of the present work. Quantifying this dynamic response, along with startup/shutdown transients, partial-load operation, and control-loop fault tolerance under fluctuating industrial thermal input, requires dedicated time-domain simulation tools (e.g., Aspen Plus Dynamics, Simulink) and constitutes a necessary and clearly identified next phase of this research program, building directly on the steady-state control architecture and design points established here.

CRediT authorship contribution statement

Mohamed Ashraf: Writing – original draft, Visualization, Validation, Methodology, Investigation, Formal analysis, Conceptualization. **Sameh Nada:** Supervision. **Hamdy Hassan:** Writing – review & editing, Visualization, Supervision, Resources, Project administration, Methodology, Conceptualization.

Consent to participate

Not applicable.

Consent for publication

This manuscript has not been submitted or published in other journals, and the authors agree to consent to publish.

Ethics approval

Not applicable.

Declaration of competing interest

The authors declare that they have no competing interests.

Acknowledgments

The authors would like to acknowledge the Mission Department of the Ministry of Higher Education (MOHE) of Egypt for providing a scholarship to conduct this study, as well as the Japan International Cooperation Agency (JICA) for offering some of the facilities, tools, and equipment and the Science, Technology & Development Funding (STDF) department which is sponsoring the research work to conduct this study under granted project No. 51418, title Innovative standalone waste heat recovery system for power generation, freshwater, and hydrogen production and storage.

Data availability

Not applicable.

References

[1] M. Nasser, T.F. Megahed, S. Ookawara, H. Hassan, A review of water electrolysis–based systems for hydrogen production using hybrid/solar/wind energy systems, Environ. Sci. Pollut. Res. 29 (2022) 86994–87018, https://doi.org/10.1007/s11356-022-23323-y.
[2] I. Dincer, C. Acar, Review and evaluation of hydrogen production methods for better sustainability, Int. J. Hydrog. Energy 40 (2014) 11094–11111, https://doi.org/10.1016/j.ijhydene.2014.12.035.
[3] J. Sigurvinsson, C. Mansilla, B. Arnason, A. Bontemps, A. Maréchal, T. I. Sigfusson, et al., Heat transfer problems for the production of hydrogen from geothermal energy, Energy Convers. Manag. 47 (2006) 3543–3551, https://doi.org/10.1016/j.enconman.2006.03.012.
[4] S. khanmohammadi, M. Saadat-Targhi, Performance enhancement of an integrated system with solar flat plate collector for hydrogen production using waste heat recovery, Energy 171 (2019) 1066–1076, https://doi.org/10.1016/J.ENERGY.2019.01.096.
[5] F. Wang, L. Wang, H. Zhang, L. Xia, H. Miao, J. Yuan, Design and optimization of hydrogen production by solid oxide electrolyzer with marine engine waste heat recovery and ORC cycle, Energy Convers. Manag. 229 (2021) 113775, https://doi.org/10.1016/j.enconman.2020.113775.
[6] J. Udagawa, P. Aguiar, N.P. Brandon, Hydrogen production through steam electrolysis: model-based steady state performance of a cathode-supported intermediate temperature solid oxide electrolysis cell, J. Power Sources 166 (2007) 127–136, https://doi.org/10.1016/J.JPOWSOUR.2006.12.081.
[7] J. Milewski, J. Kupecki, A. Szczęśniak, N. Uzunow, Hydrogen production in solid oxide electrolyzers coupled with nuclear reactors, Int. J. Hydrog. Energy 46 (2021) 35765–35776, https://doi.org/10.1016/J.IJHYDENE.2020.11.217.
[8] M. Fadel, F.M. Alelaj, H. Al-Sairfi, M. Ahmed, Adaptive fuzzy energy management of wind-battery systems with flexible desalination load, Energy Sci. Eng. (2026), https://doi.org/10.1002/ese3.70570.
[9] M.B. Ben Hamida, W. Al-Mussawi, M. Shaban, M. Marefati, Thermoeconomic optimization of a hybrid power and cooling facility using waste heat recovery from a marine diesel engine, Sci. Report. 151 (2025), https://doi.org/10.1038/s41598-025-16609-x, 15:30810-.
[10] N.M. Tahir, A.Y. Babawuro, F.M. Alelaj, B.B. Muhammad, S.S. Shitu, I.A. Umar, Control of a single-link flexible manipulator: integration of output-based filter with model predictive constraint, J. Phys. Conf. Ser. 3191 (2026), https://doi.org/10.1088/1742-6596/3191/1/012043.
[11] Press Release | Water crises threaten world peace (report) - United Nations Sustainable Development, 2026.
[12] SDG Indicators (2026).
[13] A. Firth, B. Zhang, A. Yang, Quantification of global waste heat and its environmental effects, Appl. Energy 235 (2019) 1314–1334, https://doi.org/10.1016/j.apenergy.2018.10.102.
[14] M.A. Bou-Rabee, F.M. Alelaj, H. Al-Sairfi, Quantifying the economic loss and operational implications of air pollution on grid-connected PV Systems in the Arabian Peninsula: a machine learning-based analysis, IEEE Access 14 (2026) 4180–4188, https://doi.org/10.1109/ACCESS.2025.3649764.
[15] Y. Dai, J. Wang, L. Gao, Parametric optimization and comparative study of organic Rankine cycle (ORC) for low grade waste heat recovery, Energy Convers. Manag. 50 (2009) 576–582, https://doi.org/10.1016/J.ENCONMAN.2008.10.018.
[16] H.C. Jung, S. Krumdieck, T. Vranjes, Feasibility assessment of refinery waste heat-to-power conversion using an organic Rankine cycle, Energy Convers. Manag. 77 (2014) 396–407, https://doi.org/10.1016/J.ENCONMAN.2013.09.057.
[17] B. Orr, A. Akbarzadeh, M. Mochizuki, R. Singh, A review of car waste heat recovery systems utilising thermoelectric generators and heat pipes, Appl. Therm. Eng. 101 (2016) 490–495, https://doi.org/10.1016/J.APPLTHERMALENG.2015.10.081.
[18] D. Luo, Z. Li, Y. Yan, J. Cao, H. Zhang, B. Cao, Performance analysis and optimization of an annular thermoelectric generator integrated with vapor chambers, Energy 307 (2024) 132565, https://doi.org/10.1016/J.ENERGY.2024.132565.
[19] S. Lan, Z. Yang, R. Chen, R. Stobart, A dynamic model for thermoelectric generator applied to vehicle waste heat recovery, Appl. Energy 210 (2018) 327–338, https://doi.org/10.1016/j.apenergy.2017.11.004.
[20] K. Sasaki, K. HDG, K. Sasaki, D. Horikawa, K. Goto, Consideration of thermoelectric power generation by using hot spring thermal energy or industrial waste heat, J. Electron. Mater. 44 (2015) 391–398, https://doi.org/10.1007/s11664-014-3189-z.
[21] H. Jouhara, S. Almahmoud, A. Chauhan, B. Delpech, G. Bianchi, S.A. Tassou, et al., Experimental and theoretical investigation of a flat heat pipe heat exchanger for waste heat recovery in the steel industry, Energy 141 (2017) 1928–1939, https://doi.org/10.1016/j.energy.2017.10.142.
[22] Z. Yang, J. Pradogonjal, M. Phillips, S. Lan, A. Powell, P. Vaqueiro, et al., Improved thermoelectric generator performance using high temperature thermoelectric materials, SAE Tech. Pap. 2017-March (2017), https://doi.org/10.4271/2017-01-0121.
[23] D.M. Rowe, G. Min, Evaluation of thermoelectric modules for power generation 73, 1998.
[24] M.H. Jeong, K.C. Kim, J.S. Kim, K.J. Choi, Operation of wearable thermoelectric generators using dual sources of heat and light, Adv. Sci. 9 (2022) 2104915, https://doi.org/10.1002/ADVS.202104915.
[25] M.A. Mahmoud, S. Nada, S. Mori, H. Hassan, Techno-enviro-economic evaluation of hybrid organic Rankine-thermoelectric generators integrated waste steam heat

recovery systems for power generation, J. Braz. Soc. Mech. Sci. Eng. 485 (2026), https://doi.org/10.1007/S40430-025-06229-X, 324-.
[26] Y. Tang, X. Zhao, Y. Li, A Novel Thermoelectric System for Enhancing Power Generation from Waste Heat 344, 2025, https://doi.org/10.1016/j.enconman.2025.120262.
[27] C. Liu, P. Chen, K. Li, A 500 W low-temperature thermoelectric generator: design and experimental study, Int. J. Hydrog. Energy 39 (2014) 15497–15505, https://doi.org/10.1016/j.ijhydene.2014.07.163.
[28] W. Yang, H. Xie, L. Sun, C. Ju, B. Li, C. Li, et al., An experimental investigation on the performance of TEGs with a compact heat exchanger design towards low-grade thermal energy recovery, Appl. Therm. Eng. 194 (2021) 117119, https://doi.org/10.1016/j.applthermaleng.2021.117119.
[29] R. Loni, G. Najafi, E. Bellos, F. Rajaee, Z. Said, M. Mazlan, A review of industrial waste heat recovery system for power generation with organic Rankine cycle: recent challenges and future outlook, J. Clean. Prod. 287 (2021), https://doi.org/10.1016/j.jclepro.2020.125070.
[30] R. Loni, O. Mahian, C.N. Markides, E. Bellos, W.G. le Roux, A. Kasaeian, et al., A review of solar-driven organic Rankine cycles: recent challenges and future outlook, Renew. Sust. Energ. Rev. 150 (2021), https://doi.org/10.1016/J.RSER.2021.111410.
[31] R. Loni, O. Mahian, G. Najafi, A.Z. Sahin, F. Rajaee, A. Kasaeian, et al., A critical review of power generation using geothermal-driven organic Rankine cycle, Therm. Sci. Eng. Prog. 25 (2021) 101028, https://doi.org/10.1016/J.TSEP.2021.101028.
[32] S.H. Kang, Design and experimental study of ORC (organic Rankine cycle) and radial turbine using R245fa working fluid, Energy 41 (2012) 514–524, https://doi.org/10.1016/J.ENERGY.2012.02.035.
[33] M.A. Mahmoud, S. Nada, H. Hassan, Techno evaluation of an advanced standalone system based on waste heat recovery for power, fresh water, hydrogen, and cooling, Int. Commun. Heat Mass Transfer 172 (2026) 110682, https://doi.org/10.1016/j.icheatmasstransfer.2026.110682.
[34] M.A. Mahmoud, S. Nada, S. Mori, H. Hassan, Performance evaluation of low-grade waste heat recovery for power generation via thermoelectric generators system of different configurations, Energ. Technol. 13 (2025) 1–16, https://doi.org/10.1002/ente.202402453.
[35] R. Santosh, G. Kumaresan, S. Selvaraj, T. Arunkumar, R. Velraj, Investigation of humidification-dehumidification desalination system through waste heat recovery from household air conditioning unit, Desalination 467 (2019) 1–11, https://doi.org/10.1016/j.desal.2019.05.016.
[36] R. Santosh, G. Kumaresan, G.K. Kumar, R. Velraj, Experimental parametric investigation of waste heat powered humidification dehumidification system for production of freshwater from wastewater, Desalination 484 (2020) 114422, https://doi.org/10.1016/J.DESAL.2020.114422.
[37] W. Zhu, J. Shen, X. Li, J. Zhang, Research on a two-stage humidification-dehumidification desalination system powered by the waste heat of vessel diesel engine, Appl. Therm. Eng. 281 (2025) 128546, https://doi.org/10.1016/j.applthermaleng.2025.128546.
[38] M. Morciano, M. Fasano, L. Bergamasco, A. Albiero, M. Lo Curzio, P. Asinari, et al., Sustainable freshwater production using passive membrane distillation and waste heat recovery from portable generator sets, Appl. Energy 258 (2020) 114086, https://doi.org/10.1016/J.APENERGY.2019.114086.
[39] S. Bari, T.S. Randhawa, Optimizing the design of heat exchangers to reduce the cost and maximize the production of freshwater using waste heat from a diesel-gen-set, Int J Thermofluids 14 (2022) 100142, https://doi.org/10.1016/J.IJFT.2022.100142.
[40] M.M.M. Iqbal, M.S. Javed, S. Atabay, H. Fath, M.F. Orhan, Optimization of a hybrid solar still–HDH system via parametric study for lightweight desalination in remote areas, Sci. Rep. 161 (2026) 12816-, https://doi.org/10.1038/s41598-026-43049-y.
[41] N. Lümmen, A. Karouach, S. Tveitan, Thermo-economic study of waste heat recovery from condensing steam for hydrogen production by PEM electrolysis, Energy Convers. Manag. 185 (2019) 21–34, https://doi.org/10.1016/j.enconman.2019.01.095.
[42] K. Parham, H. Alimoradiyan, M. Assadi, Energy, exergy and environmental analysis of a novel combined system producing power, water and hydrogen, Energy 134 (2017) 882–892, https://doi.org/10.1016/j.energy.2017.06.016.
[43] M. Nasser, H. Hassan, Assessment of hydrogen production from waste heat using hybrid systems of Rankine cycle with proton exchange membrane/solid oxide electrolyzer, Int. J. Hydrog. Energy 48 (2023) 7135–7153, https://doi.org/10.1016/j.ijhydene.2022.11.187.
[44] D. Elrhoul, M. Naveiro, M.R. Gómez, T.A. Adams, Thermo-economic analysis of green hydrogen production onboard LNG carriers through solid oxide electrolysis powered by organic Rankine cycles, Appl. Energy 380 (2025) 124996, https://doi.org/10.1016/J.APENERGY.2024.124996.
[45] H. Ishaq, I. Dincer, G.F. Naterer, Multigeneration system exergy analysis and thermal management of an industrial glassmaking process linked with a cu–cl cycle for hydrogen production, Int. J. Hydrog. Energy 44 (2019) 9791–9801, https://doi.org/10.1016/J.IJHYDENE.2018.12.140.
[46] M. Shaofu, E.H. Bani Hani, H. Tao, Q. Xu, Exergy, economic, and optimization of a clean hydrogen production system using waste heat of a steel production factory, Int. J. Hydrog. Energy (2021), https://doi.org/10.1016/j.ijhydene.2021.07.208.
[47] H. Noorbakhsh, Y. Aghdoud Chaboki, A. Rezvani, Optimal 4E analyses of an innovative polygeneration system for freshwater, hydrogen, and power production by waste heat recovery of ship engine and thermal energy storage, Int. J. Hydrog. Energy 127 (2025) 405–420, https://doi.org/10.1016/J.IJHYDENE.2025.03.438.
[48] Y. Lin, A.M. Sadeq, S.T. Chauhdary, S.F. Ahmad, A.Y.A. Bani Ahmad Ayassrah, A. G. Alkhathami, Multi-objective optimization and 4E assessment of a natural gas-based polygeneration system with coupling cryogenic NGL recovery, single mixed refrigerant, and hydrogen production units, Energy 344 (2026) 139843, https://doi.org/10.1016/J.ENERGY.2025.139843.
[49] W. Shaersaikai, T. Jia, A.M. Sadeq, M.K. Agrawal, T. Muhammad, S. T. Chauhdary, Modeling and thermoeconomic analysis of new polygeneration system based on geothermal energy with sea water desalination and hydrogen production, Desalination 613 (2025) 119010, https://doi.org/10.1016/J.DESAL.2025.119010.
[50] S. Alamri, A.M. Sadeq, M.A. Ahmed, M. Ayadi, J.B. Ooi, M.B. Ben Hamida, Machine learning-based optimization of an integrated system with an organic Rankine cycle, Kalina cycle, multi-effect desalination, and LNG vaporization, Energy 344 (2026) 139685, https://doi.org/10.1016/J.ENERGY.2025.139685.
[51] S. Alamri, A.M. Sadeq, M.A. Ahmed, M. Ayadi, J.B. Ooi, M.B. Ben Hamida, A novel SWOG-fueled polygeneration system integrating CO2 transcritical cycle and multi-effect desalination with thermal recovery and exergy-based evaluation through sophisticated multi-objective bat-algorithm optimization, Appl. Therm. Eng. 282 (2026) 128768, https://doi.org/10.1016/J.APPLTHERMALENG.2025.128768.
[52] M.B. Ben Hamida, A. Basem, H. Rajab, M.M. Othayq, Dynamic optimization of a solar–sCO2–CAES hybrid energy system: integration of green hydrogen production and AI-based energy management, Int. J. Hydrog. Energy 146 (2025) 149888, https://doi.org/10.1016/J.IJHYDENE.2025.06.078.
[53] American Society of Heating R and A-CE (ASHRAE), Safety Standard for Refrigeration Systems (Standard 15). Https://WwwTraneCom/Content/Dam/Trane/Commercial/Global/Learning-Center/Engineers-Newsletters/ADM-APN088-ENPdf, 2022, 2024.
[54] H. Khalil, H. Hassan, Enhancement of waste heat recovery from vertical chimney via thermoelectric generators by heat spreader, Process. Saf. Environ. Prot. 140 (2020) 314–329, https://doi.org/10.1016/j.psep.2020.05.023.
[55] T. Pujol, I. T'Jollyn, E. Massaguer, A. Massaguer, I.R. Cózar, M. De Paepe, Design optimization of plate-fin heat sink with forced convection for single-module thermoelectric generator, Appl. Therm. Eng. 221 (2023), https://doi.org/10.1016/j.applthermaleng.2022.119866.
[56] G.P. Narayan, M.H. Sharqawy, E.K. Summers, J.H. Lienhard, S.M. Zubair, M. A. Antar, The potential of solar-driven humidification-dehumidification desalination for small-scale decentralized water production, Renew. Sust. Energ. Rev. 14 (2010) 1187–1201, https://doi.org/10.1016/j.rser.2009.11.014.
[57] T. Zhao, K. Li, Y. Zhu, L. Jia, X. Hou, S. Wang, et al., An experimental method for fast evaluating thermoelectric generators using one pair of P- and N-type legs, J. Energy Resour. Technol. Trans. ASME 143 (2021), https://doi.org/10.1115/1.4050574/1104453.
[58] M. Chen, L.A. Rosendahl, T. Condra, A three-dimensional numerical model of thermoelectric generators in fluid power systems, Int. J. Heat Mass Transf. 54 (2011) 345–355, https://doi.org/10.1016/j.ijheatmasstransfer.2010.08.024.
[59] Z.G. Shen, S.Y. Wu, L. Xiao, G. Yin, Theoretical modeling of thermoelectric generator with particular emphasis on the effect of side surface heat transfer, Energy 95 (2016) 367–379, https://doi.org/10.1016/J.ENERGY.2015.12.005.
[60] Y. Zhao, S. Wang, M. Ge, Z. Liang, Y. Liang, Y. Li, Performance investigation of an intermediate fluid thermoelectric generator for automobile exhaust waste heat recovery, Appl. Energy 239 (2019) 425–433, https://doi.org/10.1016/j.apenergy.2019.01.233.
[61] G.P. Narayan, M.G.St. John, S.M. Zubair, J.H. Lienhard, Thermal design of the humidification dehumidification desalination system: an experimental investigation, Int. J. Heat Mass Transf. 58 (2013) 740–748, https://doi.org/10.1016/j.ijheatmasstransfer.2012.11.035.
[62] G.P. Narayan, M.H. Sharqawy, V.J.H. Lienhard, S.M. Zubair, Thermodynamic analysis of humidification dehumidification desalination cycles, Desalin. Water Treat. 16 (2010) 339–353.
[63] M.H. Sharqawy, J.H. Lienhard, S.M. Zubair, Thermophysical properties of seawater: a review of existing correlations and data, Desalin. Water Treat. 16 (2010) 354–380, https://doi.org/10.5004/dwt.2010.1079.
[64] K. Garg, S.K. Das, H. Tyagi, Thermal design of a humidification-dehumidification desalination cycle consisting of packed-bed humidifier and finned-tube dehumidifier, Int. J. Heat Mass Transf. 183 (2022), https://doi.org/10.1016/j.ijheatmasstransfer.2021.122153.
[65] M. Jankowski, A. Borsukiewicz, K. Szopik-Depczyńska, G. Ioppolo, Determination of an optimal pinch point temperature difference interval in ORC power plant using multi-objective approach, J. Clean. Prod. 217 (2019) 798–807, https://doi.org/10.1016/J.JCLEPRO.2019.01.250.
[66] A.N.M. Nihaj Uddin Shan, M. Zayed Mostafa, A. Hossain, M. Shadman Sakib, M. Monjurul Ehsan, Thermal assessment and optimization of process fluids in transcritical organic and transcritical CO2 Rankine cycle for waste energy recuperating system, Energy Convers. Manage.: X 15 (2022) 100258, https://doi.org/10.1016/J.ECMX.2022.100258.
[67] J.C. Hsieh, Y.C. Hsieh, Y.H. Chen, Effect of superheat degree on the performance of an organic Rankine cycle system that utilizes a wet working fluid, Energy Sci. Eng. 12 (2024) 5019–5030, https://doi.org/10.1002/ESE3.1924.
[68] T. Wang, N. Gao, T. Zhu, Investigation on the optimal condensation temperature of supercritical organic Rankine cycle systems considering meteorological parameters, Energy Convers. Manag. 174 (2018) 54–64, https://doi.org/10.1016/J.ENCONMAN.2018.08.020.

[69] G. Prakash Narayan, K.H. Mistry, M.H. Sharqawy, S.M. Zubair, J.H. Lienhard, Energy effectiveness of simultaneous heat and mass exchange devices, Front. Heat Mass Transf. 1 (2010), https://doi.org/10.5098/hmt.v1.2.3001.
[70] S.H. Soomro, A. Ullah, M.I. Soomro, M. Zulfiqar, Performance evaluation of a two-stage humidification-dehumidification desalination process, Heat Tran. (2025), https://doi.org/10.1002/HTJ.70094.
[71] A. Badgett, J. Brauch, A. Thatte, R. Rubin, C. Skangos, X. Wang, et al., Updated Manufactured Cost Analysis for Proton Exchange Membrane Water Electrolyzers, 2023.
[72] M. Ni, M.K.H. Leung, D.Y.C. Leung, Energy and exergy analysis of hydrogen production by a proton exchange membrane (PEM) electrolyzer plant, Energy Convers. Manag. 49 (2008), https://doi.org/10.1016/j.enconman.2008.03.018, 2748-file:///G:/1-Research/PAPER1 TEG Power gener.
[73] S. Khanmohammadi, P. Ahmadi, K. Atashkari, R.K. Kamali, Design and Optimization of an Integrated System to Recover Energy from a Gas Pressure Reduction Station. Prog Clean Energy, Vol 1 Anal Model, 2015, pp. 89–107, https://doi.org/10.1007/978-3-319-16709-1_6.
[74] Y.A. Çengel, A.J. Ghajar, Heat and Mass Transfer: Fundamentals & Applications, McGraw Hill LLC, 2025.
[75] R.W. Lockhart, R.C. Martinelli, Proposed correlation of data for isothermal two-phase, two-component flow in pipes, Chem. Eng. Prog. 45 (1949) 39–48.
[76] D. Chisholm, A theoretical basis for the Lockhart-Martinelli correlation for two-phase flow, Int. J. Heat Mass Transf. 10 (1967) 1767–1778, https://doi.org/10.1016/0017-9310(67)90047-6.
[77] O.L.I. Brown, The Clausius-Clapeyron equation, J. Chem. Educ. 28 (1951) 428–429, https://doi.org/10.1021/ED028P428.
[78] Y. Zhao, S. Wang, M. Ge, Y. Li, Z. Liang, Analysis of thermoelectric generation characteristics of flue gas waste heat from natural gas boiler, Energy Convers. Manag. 148 (2017) 820–829, https://doi.org/10.1016/J.ENCONMAN.2017.06.029.
[79] H. Khalil, H. Hassan, Enhancement thermoelectric generators output power from heat recovery of chimneys by using flaps, J. Power Sources 443 (2019) 227266, https://doi.org/10.1016/j.jpowsour.2019.227266.
[80] G.P. Peterson, L.S. Fletcher, Evaluation of Thermal Contact Conductance between Mold Compound and Heat Spreader Materials, 1988.
[81] T.L. Bergman, A.S. Lavine, F.P. Incropera, D.P. DeWitt, Fundamentals of Heat and Mass Transfer, 8th Edition, 8th ed, Wiley, 2018.
[82] T.L. Bergman, F.P. Incropera, Fundamentals of Heat and Mass Transfer, Wiley, 2011.
[83] M.M. Shah, A general correlation for heat transfer during film condensation inside pipes, Int. J. Heat Mass Transf. 22 (1979) 547–556.
[84] W.F. He, D. Han, W.P. Zhu, C. Ji, Thermo-economic analysis of a water-heated humidification-dehumidification desalination system with waste heat recovery, Energy Convers. Manag. 160 (2018) 182–190, https://doi.org/10.1016/j.enconman.2018.01.048.
[85] M.H. Sharqawy, M.A. Antar, S.M. Zubair, A.M. Elbashir, Optimum thermal design of humidification dehumidification desalination systems, Desalination 349 (2014) 10–21, https://doi.org/10.1016/j.desal.2014.06.016.
[86] M.A. Mahmoud, S. Nada, S. Mori, H. Hassan, Advanced tri-generation waste heat recovery system for simultaneous power, freshwater, and cooling production, Energy Convers. Manag. 353 (2026) 121180, https://doi.org/10.1016/j.enconman.2026.121180.
[87] A.R. Razmi, S.M. Alirahmi, M.H. Nabat, E. Assareh, M. Shahbakhti, A green hydrogen energy storage concept based on parabolic trough collector and proton exchange membrane electrolyzer/fuel cell: thermodynamic and exergoeconomic analyses with multi-objective optimization, Int. J. Hydrog. Energy 47 (2022) 26468–26489, https://doi.org/10.1016/j.ijhydene.2022.03.021.
[88] A.A. Fajer Alelaj, Optimization of the tilt angle of the photovoltaic module in Kuwait, in: IEEE 10th GCC Conf. Exhib., Kuwait, 2019, pp. 1–6.
[89] H. Nami, E. Akrami, F. Ranjbar, Hydrogen production using the waste heat of benchmark pressurized molten carbonate fuel cell system via combination of organic Rankine cycle and proton exchange membrane (PEM) electrolysis, Appl. Therm. Eng. 114 (2017) 631–638, https://doi.org/10.1016/J.APPLTHERMALENG.2016.12.018.
[90] S.M. Alirahmi, M. Rostami, A.H. Farajollahi, Multi-criteria design optimization and thermodynamic analysis of a novel multi-generation energy system for hydrogen, cooling, heating, power, and freshwater, Int. J. Hydrog. Energy 45 (2020) 15047–15062, https://doi.org/10.1016/j.ijhydene.2020.03.235.
[91] D.C. Bilbao, Valorization of the waste heat given off in a system alkaline electrolyzer-photovoltaic array to improve hydrogen production performance: case study Antofagasta, Chile, Int. J. Hydrog. Energy 46 (2021) 31108–31121, https://doi.org/10.1016/j.ijhydene.2021.07.016.
[92] M.G. Basiony, S. Nada, S. Mori, H. Hassan, Performance evaluation of standalone new solar energy system of hybrid PV/electrolyzer/fuel cell/MED-MVC with hydrogen production and storage for power and freshwater building demand, Int. J. Hydrog. Energy 77 (2024) 1217–1234, https://doi.org/10.1016/j.ijhydene.2024.06.211.
[93] A. Izadi, P. Ahmadi, S. Bashiri Mousavi, I. Fakhari, A comparative optimization of a trigeneration system with an innovative integration of solar heliostat towers and hydrogen production unit, Sustain. Energy Technol. Assess. 47 (2021) 101522, https://doi.org/10.1016/J.SETA.2021.101522.
[94] M. Nasser, T.F. Megahed, S. Ookawara, H. Hassan, Techno-economic assessment of clean hydrogen production and storage using hybrid renewable energy system of PV/wind under different climatic conditions, Sustain. Energy Technol. Assess. 52 (2022) 102195, https://doi.org/10.1016/j.seta.2022.102195.
[95] W.F. He, F. Wu, T. Wen, Y.P. Kong, D. Han, Cost analysis of a humidification dehumidification desalination system with a packed bed dehumidifier, Energy Convers. Manag. 171 (2018) 452–460, https://doi.org/10.1016/J.ENCONMAN.2018.06.008.
[96] O. Shamet, D.U. Lawal, S.M. Alawad, M. Antar, S.M. Zubair, Exergo-economic analysis of multi HDH system integrated with evaporative crystallizer for zero liquid discharge, Results Eng. 25 (2025), https://doi.org/10.1016/j.rineng.2025.104134.
[97] I. Bosu, H. Mahmoud, H. Hassan, Energy audit and management of an industrial site based on energy efficiency, economic, and environmental analysis, Appl. Energy 333 (2023) 120619, https://doi.org/10.1016/j.apenergy.2022.120619.
[98] A.A. Fajer Alelaj, Impact of solar irradiation on the performance ratio of the photovoltaic module, in: IEEE 10th GCC Conf. Exhib., Kuwait, 2019, pp. 1–4.
[99] S. Abo-Elfadl, M.S. Yousef, H. Hassan, Energy, exergy, economic and environmental assessment of using different passive condenser designs of solar distiller, Process. Saf. Environ. Prot. 148 (2021), https://doi.org/10.1016/j.psep.2020.10.022.
[100] B. Olateju, A. Kumar, M. Secanell, A techno-economic assessment of large scale wind-hydrogen production with energy storage in Western Canada, Int. J. Hydrog. Energy 41 (2016) 8755–8776, https://doi.org/10.1016/j.ijhydene.2016.03.177.
[101] B. Olateju, J. Monds, A. Kumar, Large scale hydrogen production from wind energy for the upgrading of bitumen from oil sands, Appl. Energy 118 (2014) 48–56, https://doi.org/10.1016/j.apenergy.2013.12.013.
[102] R.S. El-Emam, H. Özcan, Comprehensive review on the techno-economics of sustainable large-scale clean hydrogen production, J. Clean. Prod. 220 (2019) 593–609, https://doi.org/10.1016/j.jclepro.2019.01.309.
[103] M.A. Mahmoud, S. Nada, S. Mori, H. Hassan, Performance assessment of standalone hydrogen water electrolyzer production system based on waste heat power generation and humidification dehumidification system, Process. Saf. Environ. Prot. 200 (2025) 107364, https://doi.org/10.1016/j.psep.2025.107364.
[104] Planning and Engineering Data 1, Fresh Fish Handling - 4. Ice Plants, 2026.
[105] T. Longden, F.J. Beck, F. Jotzo, R. Andrews, M. Prasad, 'Clean' hydrogen? – comparing the emissions and costs of fossil fuel versus renewable electricity based hydrogen, Appl. Energy 306 (2022) 118145, https://doi.org/10.1016/J.APENERGY.2021.118145.
[106] T. Kiss, S. Popovics, Evaluation on the effectiveness of energy policies – evidence from the carbon reductions in 25 countries, Renew. Sust. Energ. Rev. 149 (2021) 111348, https://doi.org/10.1016/J.RSER.2021.111348.
[107] A.R. Abd Elbar, M.S. Yousef, H. Hassan, Energy, exergy, exergoeconomic and enviroeconomic (4E) evaluation of a new integration of solar still with photovoltaic panel, J. Clean. Prod. 233 (2019) 665–680, https://doi.org/10.1016/j.jclepro.2019.06.111.
[108] H.G. Zhang, E.H. Wang, B.Y. Fan, A performance analysis of a novel system of a dual loop bottoming organic Rankine cycle (ORC) with a light-duty diesel engine, Appl. Energy 102 (2013) 1504–1513, https://doi.org/10.1016/J.APENERGY.2012.09.018.
[109] S. Khanmohammadi, M. Saadat-Targhi, A.A.A.A. Al-Rashed, M. Afrand, Thermodynamic and economic analyses and multi-objective optimization of harvesting waste heat from a biomass gasifier integrated system by thermoelectric generator, Energy Convers. Manag. 195 (2019) 1022–1034, https://doi.org/10.1016/j.enconman.2019.05.075.
[110] T. Ioroi, K. Yasuda, Z. Siroma, N. Fujiwara, Y. Miyazaki, Thin film electrocatalyst layer for unitized regenerative polymer electrolyte fuel cells, J. Power Sources 112 (2002) 583–587, https://doi.org/10.1016/S0378-7753(02)00466-4.
[111] R. Nazerifard, M. Mohammadpourfard, R. Zarghami, A novel ORC-PEM integrated system for sustainable hydrogen production from low-grade waste heat in oil refineries, Chem. Eng. Res. Des. 223 (2025) 654–672, https://doi.org/10.1016/J.CHERD.2025.10.041.
[112] S. Ata, A. Kahraman, R. Şahin, M. Aksoy, Thermo-enviro-economic analysis of different power cycle configurations for green hydrogen production from waste heat, Energy Convers. Manag. 301 (2024), https://doi.org/10.1016/j.enconman.2024.118072.
[113] M. Nasser, T.F. Megahed, S. Ookawara, H. Hassan, Performance evaluation of PV panels / wind turbines hybrid system for green hydrogen generation and storage : energy, exergy, economic, and enviroeconomic, Energy Convers. Manag. 267 (2022) 115870, https://doi.org/10.1016/j.enconman.2022.115870.
[114] T. Hai, H.A. Dhahad, A.T.T.I.A. EA, Z. Zakaria, S. Rashidi, P. Kumar Singh, et al., Design, modeling and multi-objective techno-economic optimization of an integrated supercritical Brayton cycle with solar power tower for efficient hydrogen production, Sustain. Energy Techn. and Assess. 53 (2022) 102599, https://doi.org/10.1016/J.SETA.2022.102599.
[115] M. Nasser, M.M. Awad, A.A. Hassan, 4E assessment of all-day clean electricity generation systems based on green hydrogen integrated system using PV and PVT solar collectors and wind turbines, Int. J. Hydrog. Energy (2024), https://doi.org/10.1016/j.ijhydene.2024.05.089.
[116] O. Bamisile, D. Cai, M. Adedeji, M. Dagbasi, J. Li, Y. Hu, et al., Thermo-enviro-exergoeconomic analysis and multi-objective optimization of a novel geothermal-solar-wind micro-multi-energy system for cleaner energy production, Process. Saf. Environ. Prot. 170 (2023) 157–175, https://doi.org/10.1016/j.psep.2022.11.068.